Alma Mater Studiorum · Università di Bologna

SCUOLA DI SCIENZE
Dipartimento di Fisica e Astronomia
Corso di Laurea Magistrale in Astrofisica e Cosmologia

Identification of specific molecular species and investigation of their distribution around two deeply embedded protostars (IRAS 16293-2422) observed with ALMA

Tesi di Laurea Magistrale

Presentata da:
Francesco Grieco

Relatore:
Chiar.mo Prof.
Andrea Cimatti

Correlatore:
Chiar.mo Prof.
Jes K. Jørgensen

Sessione II
Anno Accademico 2015-2016

To my parents

Abstract

In this project I have worked with high spatial and spectral resolution data on the protostellar binary system IRAS 16293-2422 obtained with Atacama Large Millimeter-submillimeter Array (ALMA). I focused in particular on one of the two sources, IRAS 16293A, which is a Class 0 protostar, i.e. a protostar at early stages of evolution, embedded in an envelope of gas and dust which is in part being accreted by the protostar and in part being blown away through the action of molecular outflows. IRAS 16293A has a much more complicated structure than its companion, it has indeed two outflows, along NE-SW and E-W directions, and the continuum emission appears to be one at sub-mm wavelengths but split into two at mm and cm wavelengths (note that the two mm sources are different from the two cm sources). Line emission toward this source is also characterized by FWHMs much higher than those observed toward IRAS 16293B, causing some lines to blend (as I experienced).
Thus, in order to give a contribution toward the clarification of how these dynamics work, I investigated how different species are affected through studying their distribution and velocity. To do this I mapped integrated emission (Moment 0 maps) and velocity distribution (Moment 1 maps) for 33 different transitions from various species. It turned out that all species, both those who emit only from a compact region and those who also present a significant emission from the envelope, peak close to the continuum source (which represents the accretion disk) but most of the peaks present an offset towards South West, probably because of the influence of NE-SW outflow. For some species, this influence can be seen also by looking at their Moment 1 maps which show a velocity distribution resembling the one of SiO, considered to be an outflow tracer.
Moreover, using rotational diagrams, I have been able to estimate methanol temperature and column density in every pixel around Source A. The temperature map doesn't show increasing temperatures towards the center, as one would expect getting closer to the protostar, but warmer zones in the eastern and in the western part of methanol emitting region. The existence of these warmer regions can be explained with heating due to shocks generated from E-W outflow; this is a reasonable hypothesis since I observed that all methanol lines result to be blueshifted in the western warm region and redshifted in the eastern one, a probable evidence of the presence of an outflow. Furthermore, methanol transitions Moment 0 maps are characterized by the presence of a horizontally elongated structure, in the lower part of methanol emitting region. This observed structure could be the consequence of emission from methanol released into the gas phase from mantles of grains swept up by E-W outflow generated shocks.

Contents

List of Figures

List of Tables

Sommario

In questo progetto ho lavorato con dati ALMA (Atacama Large Millimeter-submillimeter Array) ad alta risoluzione spaziale e spettrale sul sistema binario protostellare IRAS 16293-2422. Mi sono concentrato in particolare su una delle due sorgenti, IRAS 16293A, che è una protostella di Classe 0, ovvero una protostella nelle prime fasi dell'evoluzione, avvolta in un inviluppo di gas e polvere che in parte viene inglobato dalla protostella e in parte viene espulso attraverso l'azione di outflow. IRAS16293A ha una struttura molto più complicata della sua compagna, essa presenta infatti due outflow, uno lungo la direzione NE-SW e l'altro lungo la direzione E-W, e l'emissione in continuo mostra una singola sorgente a lunghezze d'onda nel sub-mm mentre questa sorgente appare divisa in due a lunghezze d'onda maggiori (nel mm e nel cm). Inoltre le due sorgenti nel mm sono diverse da quelle osservate nel cm. Per quanto riguarda l'emissione in riga, questa sorgente è caratterizzata da FWHM più alte rispetto a quelle di IRAS 16293B, causando spesso un blending delle righe.
Dunque, per contribuire alla chiarificazione di come queste dinamiche funzionino, ho studiato come queste influenzino la distribuzione e la velocità di diverse specie chimiche. Per fare ciò ho mappato l'emissione integrata (Momenti 0) e la distribuzione di velocità (Momenti 1) per 33 diverse transizioni di varie specie. È risultato che tutte le specie, sia quelle emettono solo da una regione compatta sia quelle che presentano anche una significativa emissione presso l'inviluppo, hanno il picco di emissione vicino al disco di accrescimento (rappresentato dall'emissione in continuo) ma la maggior parte di questi picchi presenta un offset verso la direzione SW, probabilmente a causa dell'influenza del NE-SW outflow. Per alcune specie, questa influenza può essere vista dai Momenti 1 che mostrano una distribuzione di velocità simile a quella del SiO, considerato un elemento tracciante della presenza di outflow.
Inoltre, mediante l'utilizzo di rotational diagrams, ho potuto stimare temperatura e densità di colonna del metanolo in ogni pixel presso IRAS 16293A. La mappa della temperatura non mostra un aumento di questa verso il centro, come ci si potrebbe aspettare avvicinandosi alla protostella, ma presenta zone più calde nella parte Est e in quella Ovest della regione dove c'è emissione da parte del metanolo. L'esistenza di queste regioni calde può essere spiegata con il riscaldamento dovuto agli shocks generati dall'E-W outflow; questa è un'ipotesi ragionevole poiché ho osservato che tutte le righe del metanolo risultano essere blueshiftate nella regione Ovest e redshiftate nella regione Est, una probabile evidenza della presenza di un outflow. Inoltre, i Momenti 0 delle transizioni del metanolo

sono caratterizzati dalla presenza di una struttura allungata orizzontalmente, nella parte inferiore dalla regione dove c'è emissione del metanolo. Questa struttura che ho osservato potrebbe essere dovuta all'emissione da parte di metanolo sublimato da grani spazzati dagli shock dovuti all'E-W outflow.

Chapter 1

Introduction

IRAS 16293-2422 is a deeply embedded protostellar binary system - the first protostellar system identified as a binary and the first being classified as Class 0 (André et al. 1993) - and, during the history of its observations, it led to a better understanding of star formation both from a physical and a chemical point of view. For example in this system different complex organic molecules (COMs) have been observed. Particularly relevant is the detection by Jørgensen et al. (2012) of glycolaldehyde, the simplest sugar, which plays a fundamental role in the formation of biologically relevant molecules. Thus the study of distribution of COMs and other species helps to formulate models on their formation and could lead to understanding how life was born in a sun-like star system.

I have worked with new ALMA data to study the distribution and dynamics of different species toward this system, focusing in particular on IRAS 16293A. It is an interesting object to study because of its complicated structure: its continuum source appears to be one at sub-mm wavelengths but it splits into two at mm and cm wavelengths; moreover it presents two molecular outflows and its lines are much wider than those emitted towards IRAS 16293B. In this project I try to understand if a species is more concentrate toward the envelope or the hot corino of the forming star, or if they are influenced by outflows. I have focused particularly on the distribution of methanol and on its temperature distribution (obtained through rotational diagrams) since methanol is an important molecule in the reaction schemes which lead to the formation of more complex species (Caselli and Ceccarelli 2012).

Before the description of my work, in the following paragraphs is presented an introduction about star formation and a summary on what is known about IRAS 16293-2422.

1.1 Prestellar phase

More than 80 % of the molecular gas in the Milky Way is located in molecular clouds in which it is estimated that a total of 2 $M_{\odot} yr^{-1}$ form. Molecular gas - mainly composed of

H_2 - contained in these clouds is usually at temperatures of $\approx 10K$.
At big scales we have Dark Clouds - with diameters of tens of parsecs, masses between $10^2 M_\odot$ and $10^5 M_\odot$ and densities of $10^3 cm^{-3}$ - so called because they block light coming from background stars, thus appearing dark at optical wavelengths (see Figure 1.1). This happens because they contain dust grains which block radiation with wavelengths shorter then their dimension ($\approx 1\mu m$). The presence of dust grains is also responsible for shielding the inner parts of the cloud from the radiation coming from close by stars, preventing the molecules to dissociate.

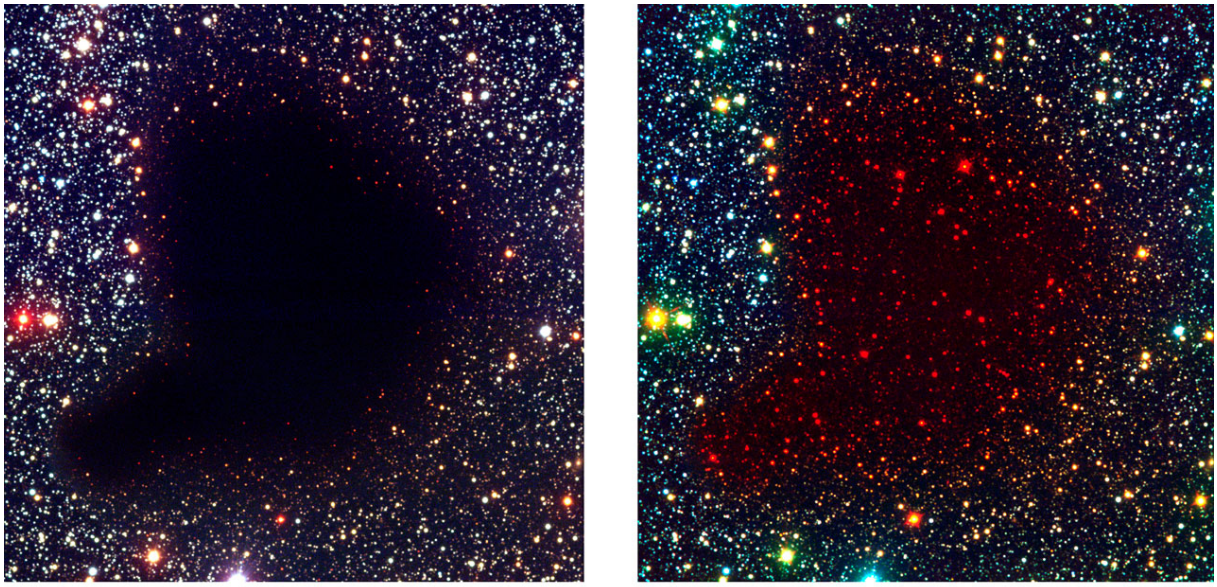

Figure 1.1: Left: Image of a Dark Cloud at visible and near-infrared wavelengths. Right: Same Dark Cloud observed at visible, near-infrared and infrared wavelengths. Here one can appreciate how shorter wavelengths are absorbed by dust grains in the cloud while wavelengths longer than grains dimensions manage to pass across, thus in the infrared band it is possible to observe stars behind the cloud.

At smaller scales, molecular gas is concentrated in denser regions ($n \approx 10^4 cm^{-3}$), called Dense Cores, around 0.1 pc large and having masses around 10 $M_\odot$.

It has been measured that molecular clouds have average age of $\approx 10^7 yr$ while their free fall time is estimated to be smaller by an order of magnitude; that means that there must be forces which oppose to the collapse of a cloud (Stahler and Palla 2004). Theories show that to have such massive Dark Clouds - which in the case of masses of $10^5 M_\odot$ are called Giant Molecular Clouds - at hydrostatic equilibrium as those we observe, thermal pressure is not sufficient to oppose to gravity, so it must be due to other contributions. At equilibrium, virial theorem is:

$$0 = 2K + W + 2U + \mathcal{M} \tag{1.1}$$

where W is the gravitational energy, U is the internal energy, $\mathcal{M}$ is the magnetic energy and K is the kinetic energy of the gas of the cloud. K is given by the sum between the kinetic energy corresponding to rotation and the one corresponding to turbulent motions ($K = K_{rot} + K_{turb}$). It can be proved that, for Dark Clouds, $\frac{2U}{|W|} << 1$, meaning that internal energy is not able to prevent the collapse, as previously said. Same for rotational kinetic energy: $\frac{2K_{rot}}{|W|} << 1$. Magnetic energy and turbulent kinetic energy, on the other hand, seem to be comparable to gravitational energy. So the equilibrium is more likely to be due to these contributions, even though is not still completely clear what is the process sustaining turbulence in molecular clouds.

In Dense Cores, instead, we have that $\frac{2U}{|W|} \approx 1$ so hydrostatic equilibrium condition can be well described with Bonnor-Ebert theory, considering only gravity and thermal pressure. This theory predicts that, at hydrostatic equilibrium, the gas of a self gravitating, isothermal and spherical cloud has the density profile shown in Figure 1.2; so density increases towards the center.
It can be proved that lighter Dense Cores would be unstable without non-thermal energies; anyway they are modeled as thermally supported, because other contributions - for Dense Cores - are much less important compared to the thermal one.

With their simulations, Keto and Caselli (2008) determined, for Dense Cores with masses between $1M_{\odot}$ and $10M_{\odot}$, a critical density for dynamical stability of $10^5 cm^{-3}$. If all the gas is at densities lower than this quantity, the whole Dense Core cools mainly by molecular line radiation and can be considered isothermal. These Dense Cores turn out to be stable so - unless there are significant changes in their environment - they don't collapse and don't give birth to stars.

If, instead, there are regions in the core where density reaches values higher than $10^5 cm^{-3}$, here the gas will cool principally by collisional coupling with the dust; this is likely to happen in the inner regions because of the density profile predicted by Bonnor-Ebert theory. Moreover, since dust is heated by radiation coming from surrounding stars, it results cooler towards the center of the core. Consequently, gas will also show a radial temperature gradient, being it coupled to dust at the center and cooling by molecular line radiation elsewhere.
It is in this type of Dense Cores, also called prestellar cores, unstable to collapse, that star formation takes place.

1.2 Protostellar phase

From the start of the collapse of the prestellar core to the formation of a star it takes a few million years (Stahler and Palla 2004).
Protostars are divided into 4 classes, each one representing a different stage of the evolution: from a stellar core accreting material from the cloud in which it is still deeply

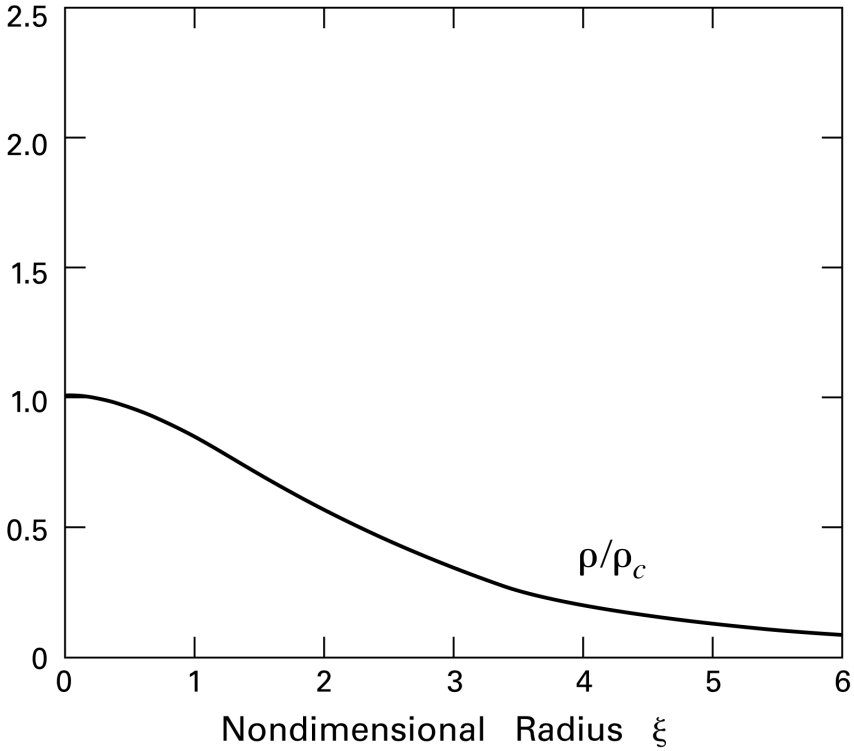

Figure 1.2: Density profile in a Bonnor-Ebert sphere (from Stahler and Palla 2004). ρ_c is the density at the center and ξ is the nondimensional radius defined as $\xi = r\sqrt{\frac{4\pi G\rho_c}{c_s^2}}$.

embedded, to a formed star which has already accreted - or blown away through outflows (see §1.2.2) - the majority of the forming material and it is not obscured by it anymore. Here I will give a description of the evolution mechanisms of a protostar and then I will display the observational differences between the classes, summarized in Figure 1.3.

During the first part of the collapse, the core is optically thin at infrared wavelengths and radiation is therefore allowed to escape; this permits the core to keep the same temperature. Thus the first part of the collapse can be considered isothermal. Density increases and at some point the gas becomes so opaque that radiative cooling is not efficient anymore and temperature in the core increases: the core entered a phase of adiabatic collapse which lasts until thermal pressure is high enough to stop the collapse. This hydrostatic core is only quasi-stable because radiation can still escape from outer regions, the core keeps contracting and temperature keeps increasing. When it reaches temperature of $\approx 2000K$, H_2 molecules dissociate absorbing thermal energy and therefore causing the break of hydrostatic equilibrium; a new phase of collapse starts until hydrostatic equilibrium is reached again. Protostars which are in one of the above-mentioned phases are classified as *Class 0* protostars whose observational features, as well as for other classes,

are summarized in §1.2.1. Class 0 phase lasts approximately $10^4 yr$.
The *Class I* phase follows. It lasts around $10^5 yr$ and it is the phase during which the protostar - i.e. the hydrostatic core formed at the end of Class 0 phase - accretes most of the surrounding material. However, great part of the infalling envelope doesn't fall directly on the protostar: because of its high angular momentum some material first falls into the equatorial plane forming a disk (accretion disk), and then it spirals towards the protostar. Of course, the accretion disk doesn't suddenly form during this main accretion phase, but it starts forming already during Class 0 phase. The spiraling can happen because the material in the disk loses angular momentum via outflows which characterize Class 0 and I protostars (more on this in §1.2.2).
During following phases - *Class II* and *Class III* phases - more infalling and removal of circumstellar material takes place.

1.2.1 Observational classification of protostars

- *Class 0*: Protostars belonging to this class are the most extinguished and embedded in their envelope and present energetic outflows. They peak at sub-mm and far-infrared wavelengths with a SED which is the one of a single black body having a temperature of around 20-30 K (see e.g. Lada 1999). This is more likely to be representative of the emission of gas cloud in which the protostar is embedded than the emission of the protostar itself.

- *Class 1*: These sources also present outflows but less energetic than Class 0 protostars and, although less extinguished and embedded, they are still featured by a large infalling envelope of gas and dust. Class 1 sources peak at sub-mm and far-infrared wavelengths showing SEDs broader than a single black body. This is due to an infrared excess caused by the emission of circumstellar dust: we have different dust temperatures depending on the distance from the center causing the infrared part of the SED to be the result of the superimposition of different black bodies emissions. Class 1 SEDs are also characterized by silicate absorption at $\approx 10\ \mu m$ wavelengths.

- *Class 2*: Class 2 protostars peak in near-infrared or visible wavelengths. The infrared excess, less intense than for Class 0 sources, shows a power-law trend towards longer wavelengths and it is due to emission from dust at different temperatures present in the accretion disk. When observed at at optical wavelengths, Class 2 sources have the same spectra characteristics of Classic T-Tauri stars (CTTS), featuring Hydrogen emission lines and different forbidden lines. They don't show evidence of outflows.

- *Class 3*: Class 3 sources feature single black body SEDs which peak in optical or infrared wavelengths. These protostars are generally free of circumstellar dust and gas and are therefore non extinguished by it. However, it can be present extinction

from foreground dust which cannot easily be recognized since extinction would cause a trend ($F_\nu \propto exp(-\nu)$) similar to the one typical of the high frequency side of a black body ($F_\nu \propto exp(-\frac{h}{kT}\nu)$).
Since they don't show emission of strong lines, they are likely to be classified as Weak-lined T-Tauri stars (WTTS). Their SEDs are also featured by a strong and variable X-ray emission.

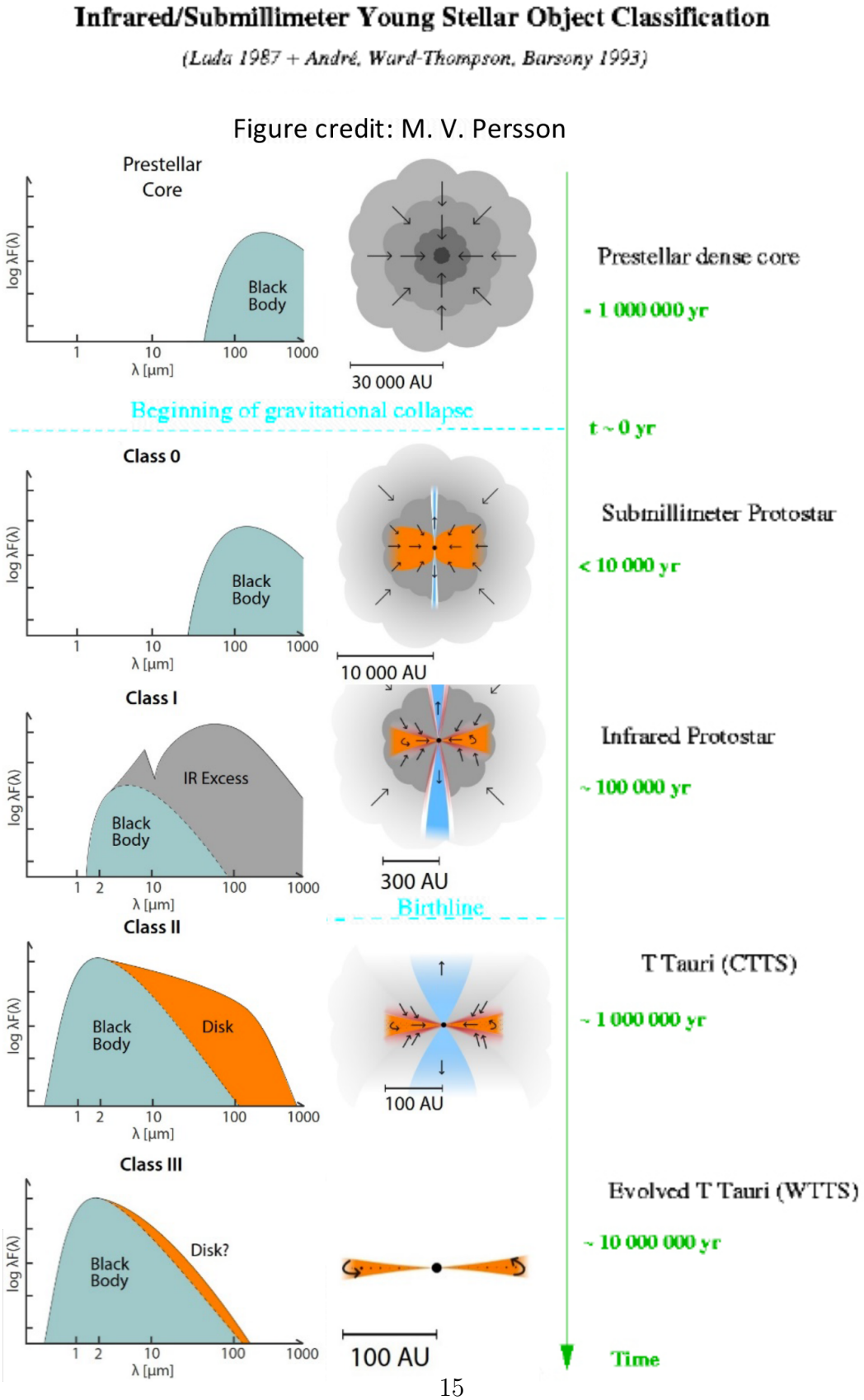

Figure 1.3: Young Stellar Object classification.

1.2.2 Formation of outflows and their role in the evolution of a protostar

As aforesaid, protostars evolve from Class 0 to III by removing the infalling envelope and the circumstellar disk. One could think that accretion alone could be enough to explain the clearing of the surroundings of a protostar, meaning that all the envelope material would be converted in stellar mass. But prestellar core are generally much more massive than the stars which form inside of them (see e.g. Lada 1999), so there must be a part of the envelope which is not accreted by the protostar but removed by some process. This process is thought to be molecular outflows which could also provide a source for sustaining turbulence in molecular clouds (see §1.1). But how do these outflows form? First, to have material in the disk spiraling towards the protostar, it must lose angular momentum and energy so there must be some wind originating from the disk ejecting material. Second, accretion disks have keplerian velocity trend so the infalling material from the disk, when it is accreted by the protostar, has significantly higher angular momentum than the protostar causing an acceleration if its rotation. At some point, equatorial velocity of the star will reach a value high enough that centrifugal forces don't allow any further accretion. Because of this, there must be also an ejection of material from the protostar through winds that allow it to lose angular momentum. So, in order to keep accreting more material, the protostar has to eject material at the same time. How these winds are generated is still not completely clear. An example of outflow is shown in Figure 1.4.

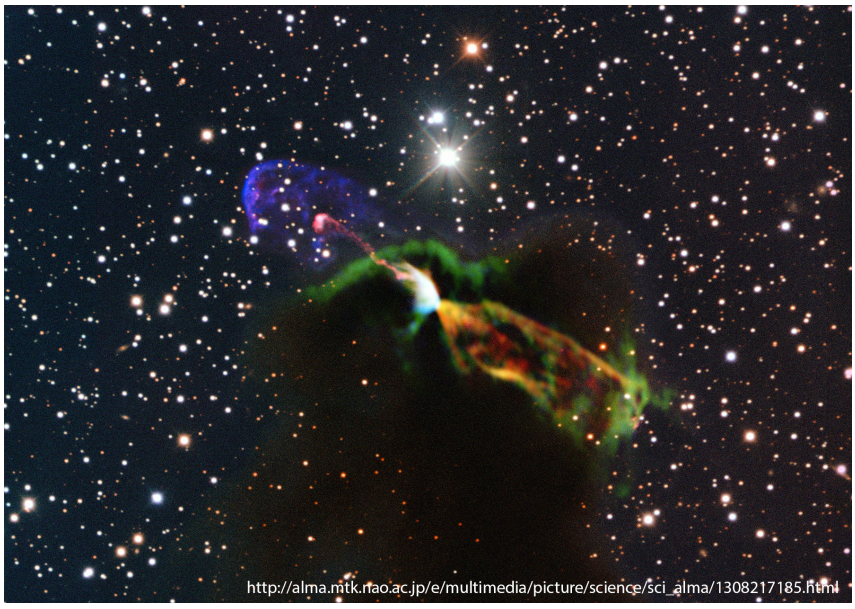

Figure 1.4: Molecular outflow ejected by a protostar. Combination of observations acquired at sub-mm (orange and green) and visible (pink and purple) wavelengths.

$X + Y \rightarrow XY + h\nu$	Radiative association
$XT + h\nu \rightarrow X + Y$	Photodissociation
$XY^+ + e \rightarrow X + Y$	Dissociative recombination
$X^+ + YZ \rightarrow XY^+ + Z$	Ion-molecule reaction
$X^+ + YZ \rightarrow X + YZ^+$	Charge-transfer reaction
$X + YZ \rightarrow XY + Z$	Neutral-neutral reaction

Table 1.1: Gas phase chemical reactions.

Protostellar phase starts therefore with a Class 0 protostar, deeply embedded in its envelope, with an accretion disk from whom winds generates, giving rise to molecular outflows which blow away some of the envelope. These winds get progressively less intense, thus Class I protostars blow away their remaining envelope with less energetic outflows, and Class II and III objects don't present outflows at all. Further removal of the envelope, i.e. the transition from Class II to III, is more likely to be due to accretion only.

On the effect of molecular outflows on the chemistry of the environment surrounding a protostar see §1.3.4.

1.3 Chemistry of Young Stellar Objects

In this section I am going to illustrate some basic chemical processes - both gas phase and grain surface processes - occurring in molecular clouds which involve some of the species I observed during this project. Then, I will describe the chemical distribution around Class 0 protostars and how it is influenced by outflows.

1.3.1 Gas phase chemistry

The few molecular processes occurring in the gas phase which give rise to all known reactions are listed in Table 1.1 (see Van Dishoeck and Hogerheijde 1999). Note that only two-body processes are listed because three-body processes are not important in ISM except for dense gas near stellar photospheres (i.e. where $n \approx 10^{11} cm^{-3}$).

Photodissociation is important in photon-dominated regions where molecules are destroyed by absorption of UV photons; this happens at the edge of dark clouds (as mentioned in §1.1) because of the emission by close by stars, while the internal region are shielded by dust grains which absorb and scatter this radiation. Moreover, in dense clouds, molecules can be destroyed by ion-molecules reactions and, in regions of particularly high temperature and density such as those affected by shocks, also by collisional dissociation. As regards associations, it is to be noted that at low temperatures associations by ion-molecule reactions are faster compared to neutral-neutral association, due to

the long-range attraction between ions and molecules.

Being H and H_2 very abundant, they play a fundamental role in reactions. But this is only under particular circumstances. For example, at low temperatures, only reactions with small ions are exothermal and thus significant. Under this condition, it is also important for ion-molecule reactions the role of H_3^+ which forms by reactions between H_2 and H_2^+ (H_2^+ is formed by ionization of H_2 by cosmic rays). Instead, at higher temperatures - between 200 and $2000K$ - neutral-neutral reactions with H and H_2 occur. This happens, for example, in the inner zones of Class 0 protostars, the hot corinos (see §1.3.3), where great part of the remaining O in the gas phase is converted into H_2O by reactions $O + H_2 \rightarrow OH + H$ and $OH + H_2 \rightarrow H_2O + H$ starting already at few hundreds K. Already during prestellar phase, formation of CO in the deeper regions of the cloud via $C^+ \rightarrow O$ transition, causes a decrease of O. So with the decreasing of oxygen in hot corinos, abundances of species destroyed by oxygen are enhanced. Before they are locked in CO, C and C^+ lead to the formation of molecules such as CN, HCN, CS and complex carbon chains.

1.3.2 Grain surface chemistry

To explain abundances - or just the existence - of certain molecules in ISM, it has been necessary to introduce models considering also reactions occurring on the surface of dust grains, besides gas phase reactions. Perhaps the most important example of molecule which mainly forms on dust grains is H_2; its abundances couldn't be explained otherwise. But a vast number of species are produced on grain surfaces. I will here explain the formation mechanism of some of them.

First, let's give an overview of the composition of mantles of dust grains. They are not homogeneous but consist of a core of silicates, surrounded by layers of polar ices - mainly formed of H_2O with minor amounts of CO_2, CO, CH_4 and CH_3OH - and apolar ices - containing mostly CO, some O_2 and N_2 and a small amount of H_2O.
For densities $\geq 10^5 cm^{-3}$ - which is the critical value to start the collapse (see §1.1) - time scale for depletion is minor than the free fall time, so freezing out of molecules on dust grains is relevant all over the envelope of Young Stellar Objects. At lower densities, for example at the edges of a cloud, mostly polar ices form due to the large abundance of H, while in inner regions, at higher densities, we have mostly apolar ices. During the collapse which leads to the formation of the star, different layers form because grains pass through zones of increasing density, so polar ices condense first, already at low densities, and apolar ones follow forming a crust upon the polar layer. Moreover, apolar ices sublimate more easily than polar ices so proceeding towards inner regions of the envelope - i.e. at higher temperatures - we find mantles made mainly of polar ices. At the most inner regions we don't find mantles at all because all species sublimated. The situation

is summarized in Figure 1.5 from Van Dishoeck (2014). See also §1.3.3.

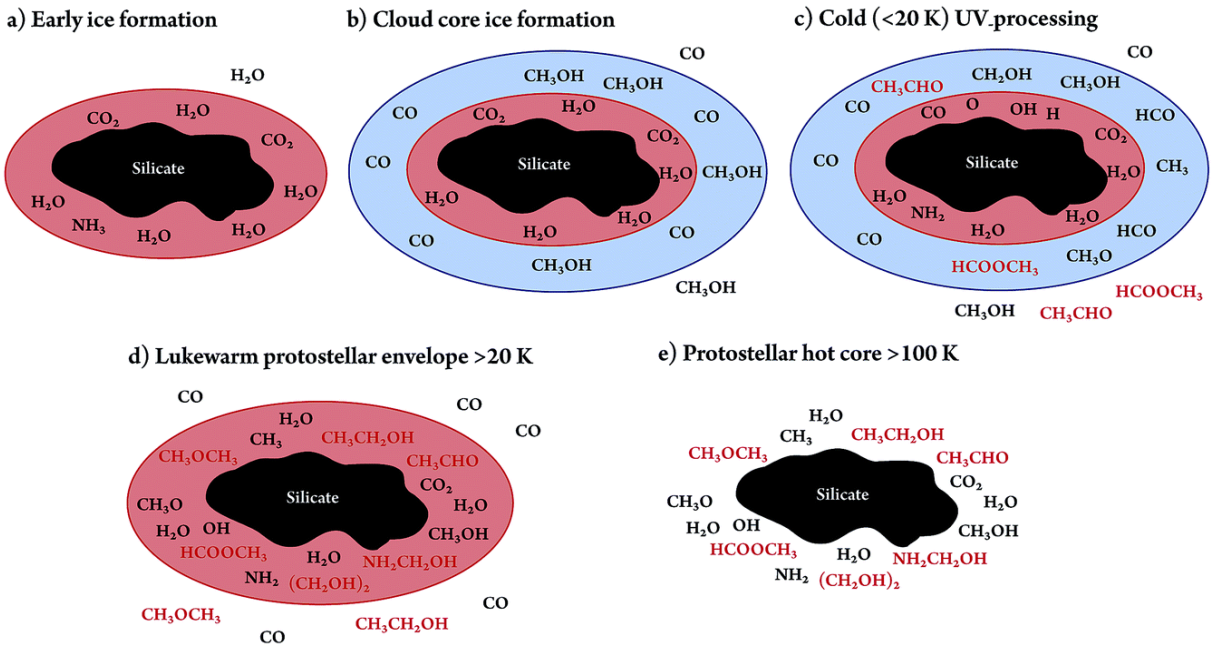

Figure 1.5: Image from Van Dishoeck (2014) representing the different phases of formation of ices on dust grains and their sublimation at different conditions during star formation.

After molecules landed on dust grains, they diffuse on their surface and give rise to reactions. As previously mentioned, H is very abundant so grain surface reactions lead mainly to the formation of hydrogenated species like H_2O, NH_3 and CH_4. While the most accreted molecule is CO (as aforesaid H_2 forms mainly on grains instead) which plays a fundamental role in the formation of CH_3OH via hydrogenation and other molecules as shown in Figure 1.6.

Due to the heating by the protostar, grain mantles sublimate when they reach proper temperature - depending on their composition - and release molecules in the gas phase whose emission lines can therefore be observed. Thermal sublimation is relevant only for temperatures $\geq 20K$, but there are also non-thermal mechanisms which cause the release of molecules in the gas phase also at lower temperatures. These are grain-grain collisions, UV absorption (for example as it happens to grain at the edge of dark clouds, which are exposed to UV radiation coming from close by stars), cosmic rays and heating due to photons emitted by the formation of molecules on grains surfaces. For example, they observed CH_3OH in the gas phase already in prestellar cores (Bacmann et al. 2012) - indicating that methanol might form already during prestellar phase - and the release of this species at temperatures as low as $\approx 10K$ means that the sublimation is likely to be non-thermal.

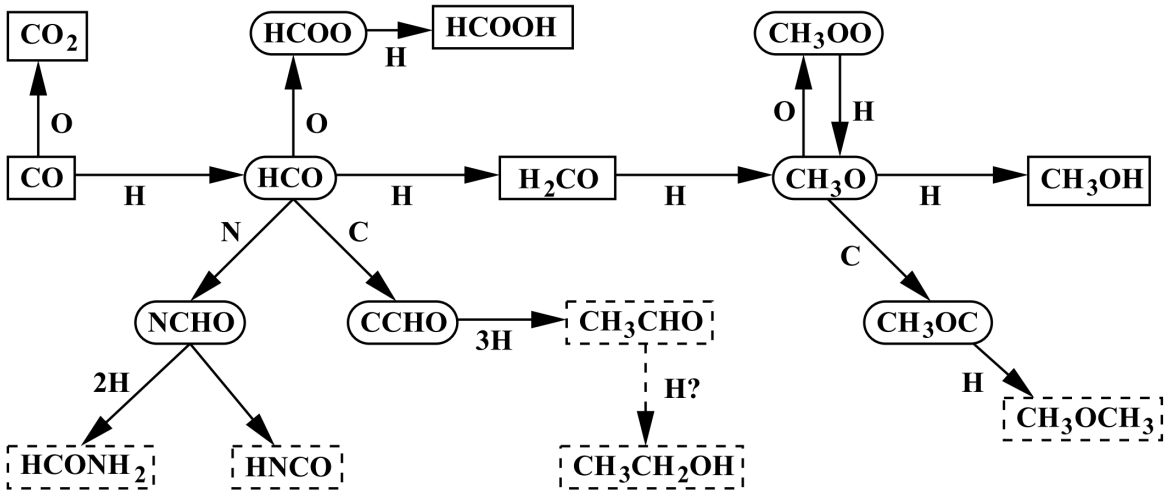

Figure 1.6: Image from Tielens and Hagen (1982). Here are displayed hydrogenation reactions which lead from CO to the formation of CH_3OH and other reactions which form complex hydrocarbons on the surface of dust grains.

1.3.3 Chemistry of Class 0 protostars

IRAS 16293-2422 is a system of two deeply embedded protostars (more on it in the next paragraph) belonging to Class 0. It is necessary to spend some words on the distribution of chemical species around Class 0 protostars then.
During the collapse, density and temperature of the gas increase towards the center as gravitational energy is converted into radiation(see §1.2). This trend, for IRAS 16293-2422, is reported in Figure 1.7 from Crimier et al. (2010).

At big scales ($\geq 100AU$) the whole star forming system can be seen as a spherical envelope heated from the forming star inside it, but at smaller scales the structure is more complicated due to the presence of a forming disk or - as in the case of our system - multiple sources. Inside it, we can identify four zones (also shown in Figure 1.7) characterized from the presence of different chemical species, due to higher temperatures and densities as we get closer to the center[1]. These four zones are:

Zone i): Same composition of the molecular cloud from which the collapse started. There is no appreciable presence of frozen species.

Zone ii): Molecules freeze-out on dust grains. In particular in this zone, defined by a dust temperature lower than 22 K, CO freezes out so this is a CO depleted zone.

The extent and the existence of zones i) and ii) depends on density and age of the collapsing protostar. At early ages and too low densities, there could be no significant freeze-out of molecules on dust grains thus no existence of zone ii). At

[1]See Caselli and Ceccarelli (2012).

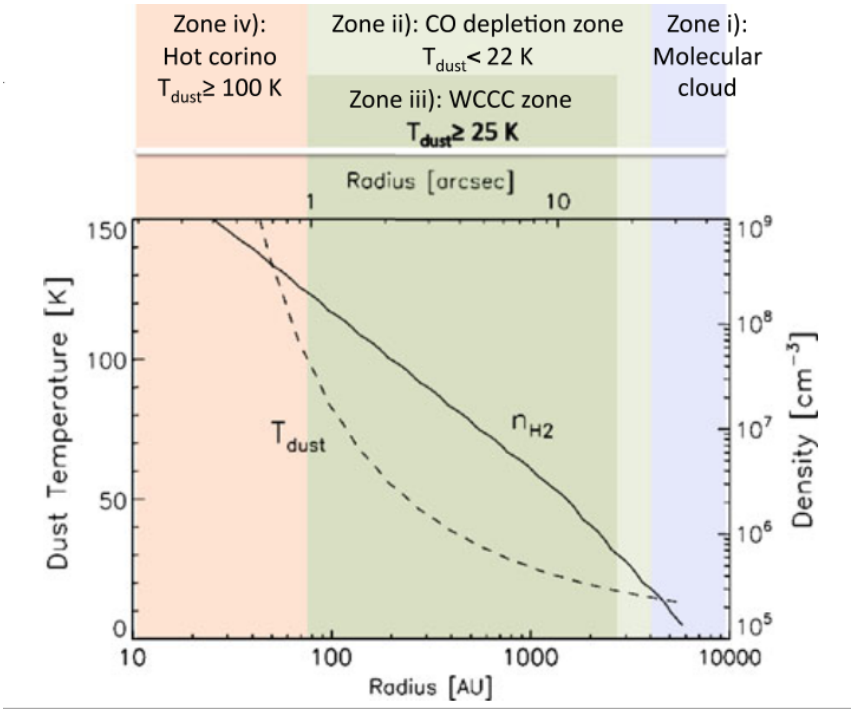

Figure 1.7: Temperature and density profile of IRAS 16293-2422 and chemical zones from Crimier et al. (2010).

late stages of the collapse instead, in the outer region, there could be almost no more gas which has the same composition of the dense core anymore because the freeze-out has become very important even in this region.

Zone iii): By moving into inner regions, we find dust characterized by higher temperatures. When dust temperature is over around 25 K, methane (CH_4) sublimates from grains starting the formation of more complex C-chain molecules which have been observed. This is called Warm Carbon Chain Chemistry (WCCC) region.

The existence of this zone depends on the abundance of frozen CH_4 on dust grains, i. e. on the efficiency of its formation during the prestellar phase.

Zone iv): At temperatures above 100 K all species on dust grains sublimate, thus a great variety of molecules - such as methanol and complex organic molecules - are observed in this zone. The zone is known as hot core, for high mass protostars, or hot corino, for low mass protostars like IRAS 16293-2422. Hot corinos are smaller in size and have a lower temperature compared to hot cores, this affects their chemical abundances which are very different from hot cores. Moreover, also for this zone, the composition of ices which sublimate is important and also explains the differences in chemical abundances from source to source.

1.3.4 Outflows impact on the medium around YSO

As already pointed out in §1.2, protostellar phase is also characterized by the presence of outflows which allow the material of the circumstellar disk to lose angular momentum and make it fall towards the protostar. Outflows give rise to shocks which have an impact on the medium they sweep up, i.e. they heat up gas and sputter dust grains. $50 km/s$ shocks are enough to completely destroy the mantles causing a significant increase in the abundance of species like CH_3OH - which is one of the most abundant in mantles - in the gas phase. It has been indeed observed that these regions show a composition similar to hot cores and hot corinos. These shocks are also energetic enough to partially erode the core of the grain (a $100 km/s$ would be needed to completely destroy the grain) and thus also species like Si, Fe are released. Once in the gas phase, Si can react with OH and H_2 to produce SiO which is therefore a tracer of outflows.

For a description of species distribution toward IRAS 16293-2422 see Figure 1.9 in the next paragraph.

1.4 IRAS 16293-2422

IRAS 16293-2422 is the first protostellar system identified as a binary and is located in the eastern part of the ρ Ophiuchus cloud complex at a distance of 120 pc (see e.g. Loinard et al. 2008). The two components, IRAS 16293A and IRAS 16293B, are at a distance of 620 AU from each other (Chandler at al. 2005), both presenting compact millimeter continuum emission (see Figure 2.4) - an evidence of the presence of disk structures around them - and embedded in a $3 M_{\odot}$ common envelope of size $\approx 3000 AU$ (Schöier et al. 2004; Correia et al. 2004). This is also the first system where glycolaldehyde, the simplest sugar, a molecule which plays a fundamental role to the formation of biologically relevant molecules, has been detected (see Jørgensen et al. 2012).
It has been confirmed that IRAS 16293A is a Class 0 protostar, whereas it is still uncertain if IRAS 16293B is a very young object as well or if it is in a more evolved state, probably T-Tauri (see e.g. Pineda et al. 2012). In this project I focused mainly on IRAS 16293A.

While the continuum emission map obtained in this work - at sub-mm wavelengths - shows only one continuum source for IRAS 16293A, at longer wavelengths (1 mm) Source A turns out to be split into two continuum sources denoted as Aa (which coincides with the continuum source observed at sub-mm wavelengths) and Ab. So Source A could be a binary itself which components are separated by a distance of about 120 AU (see Figure 1.8 from Chandler et al. 2005).

The centimeter continuum emission is also divided into two sources (Wootten 1989) - different from those observed at 1mm - denoted A1 (East) and A2 (West) and indicated in Figure 3.4. Toward Source A it has been put in evidence the presence of two outflows:

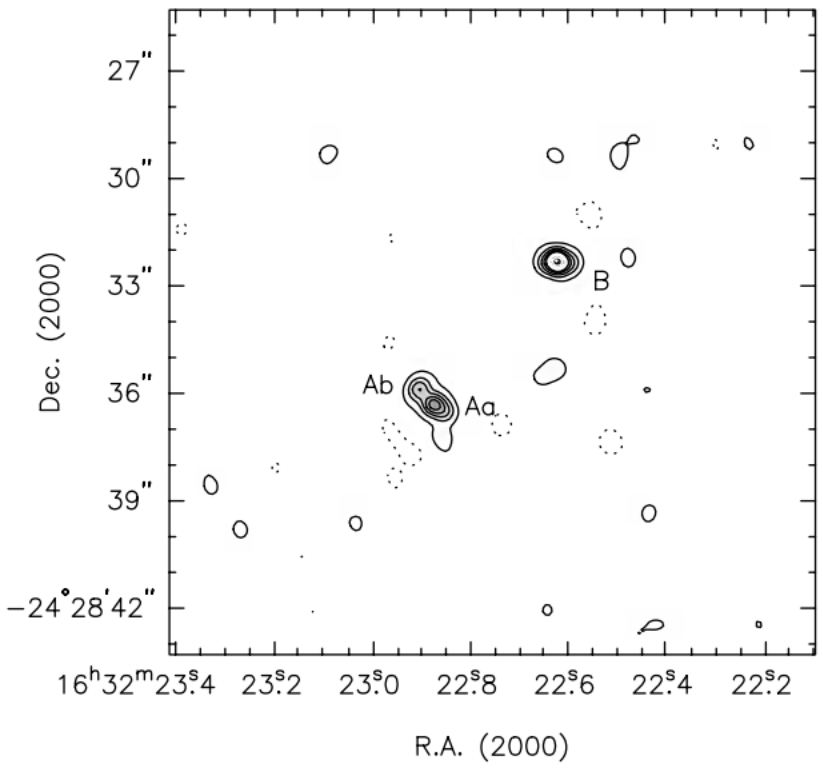

Figure 1.8: 1 mm continuum image from Chandler et al. (2005). IRAS 16293A continuum emission is resolved in two components: Aa and Ab.

one along the North East - South West direction, one along the East - West direction (see e.g. Loinard et al. 2013). Thus, we can see that Source A has a much more complicated structure than Source B, and its spectrum is harder to analyze, too. It is in fact characterized by much broader lines compared to Source B which therefore often blend. For IRAS 16293A we have FWHMs up to $10 km/s$ while for IRAS 16293B their values are around $\approx 1.5 km/s$ (see Tables 3.2, 3.3 and 3.6 and Appendix B).

As said in §1.3.3, in different areas we can observe the emission of various species due to different dust temperatures and formation histories of the sources (i.e. different composition of the ices around the sources). In Figure 1.9 from Caselli and Ceccarelli (2012) is summarized the distribution of the molecules in IRAS 16293-2422 as obtained from single dish and interferometer observations respectively by Caux et al. (2011) and Jørgensen et al. (2011). Here we can see how simplest molecules (in group I in the image) are more concentrated in the cold envelope, molecules such as CH_3OH or H_2CO are present towards both sources and the cold envelope (group IV), complex organic molecules are more concentrated toward Source B (group III)[2] and N- and S- bearing

[2]Even if more recent studies have detected the presence of such species also toward Source A (see e.g.

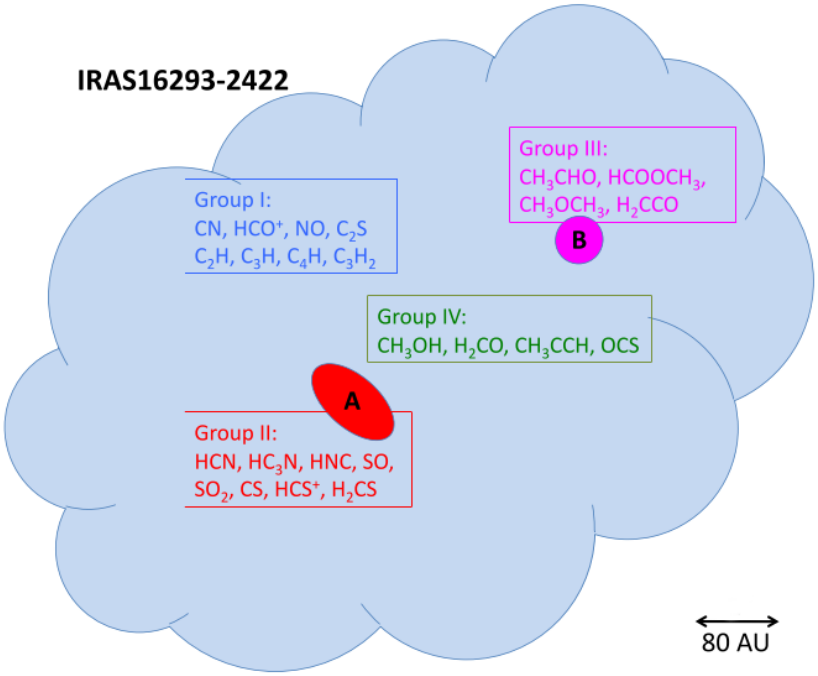

Figure 1.9: Summary of species distribution in IRAS 16293-2422 (from Caselli and Ceccarelli 2012).

molecules toward Source A (group II). The different concentration of species towards the two sources probably means that they have different masses and luminosities. This would cause the temperatures in the gas and dust close to them, and thereby also the chemistry, to differ.

Jørgensen et al. 2016).

Chapter 2

Data Analysis

2.1 ALMA and the PILS dataset

Figure 2.1: The Atacama Large Millimeter/submillimeter Array (ALMA).

As said in §1.2, Class 0 protostars continuum emission peaks in sub-mm. Most of emission lines due to transition between rotation levels in molecules are located in the sub-mm band as well. For this reason many single-dish and interferometer observations were carried in this band. The new high spatial and spectral resolution data I worked with in this project were obtained with the ALMA telescope.

Following I give a description of ALMA telescope and some specifics about this observation.

The Atacama Large Millimeter/submillimeter Array (ALMA) is an interferometer working in mm and sub-mm bands (between 84 and 950 GHz) composed of 66 antennas which are divided into two groups:

1. a main array of 50 antennas with a 12 m diameter, made to obtain high angular resolutions thanks to the possibility to dispose the antennas on baselines between 150 m and 16 km long;

2. a compact array (Atacama Compact Array, ACA) composed of 12 antennas with a 7 m diameter and 4 antennas with a 12 m diameter. The 7m antennas can have smaller baselines - between 9 m and 30 m - which means increasing the largest observable angular scale. So ACA is complementary to the main array.

Every receiver mounts two dipoles, perpendicular one to the other, to detect components of signals polarized along the directions of the two dipoles orientations.

This observation of IRAS 16293-2422 was part of the "Protostellar Interferometric Line Survey (PILS)" presented in Jørgensen et al. (2016). During the observation, typically 36-41 12 m antennas from the main array and 8-10 7 m antennas from ACA were active. The ALMA's Band 7 part of the survey, which is the one that produced the dataset I worked with, comprehends a range of frequencies from 329.147 GHz to 362.896 GHz. This range has been covered using 18 spectral settings, each one covering a bandwidth of 1875 MHz (4 spectral windows 468.75 MHz wide).

The spectral resolution, i.e. the width of each channel, is of 0.244 MHz ($\approx 0.2\ km\ s^{-1}$) and each channel is characterized by an rms of about $7 - 10\ mJy\ beam^{-1}$ implying a sensitivity approximately two order of magnitudes better than any previous study. The images in the datacubes I worked with (see next paragraph) were produced - after a calibration and cleaning process - with a circular restoring beam having a diameter of 0.5" ($\approx 60\ AU$).

2.2 Analysis

In the project, I have been working with datacubes - i.e. cubes of 1917 bidimensional images, one for each channel, disposed along the velocity/frequency axis - from which continuum emission has been subtracted. Throughout these datacubes I have identified 33 different emission lines (in a dataset containing hundreds of lines) from different species

toward Source A and fitted them with Gaussian functions. For each line I have created Moment 0 (integrated intensity) and Moment 1 (velocity) maps and I have also used $^{13}CH_3OH$ lines to make rotational diagrams to get its temperature and column density in each pixel. All results are shown and discussed in Chapter 3.
All this has been done in order to investigate the distribution and dynamics of different species in the gas of this star forming system: e.g. to understand whether a certain species emission is more concentrated towards the accretion disk or towards the envelope, or to understand if it is influenced by the presence of outflows - for example by looking at its temperature distribution, as I did for ^{13}methanol and methanol, obtained from rotational diagram.
In the following paragraphs I am giving a little description about Moment maps and rotational diagrams and about how I worked to obtain them.

I have used the software CASA 4.5.2 for realizing moments and gaussian fits and I have manipulated CASA's outputs using Python 2.7.6 .

2.2.1 Moments and statistics

Moment 0 of an image consists of integrated emission maps obtained by integrating the flux along the velocity axis, over the width of the line, for each pixel:

$$M_0 = \int_{v_i}^{v_f} S_v dv \qquad . \tag{2.1}$$

The Moment 1 maps show the mean velocity of emitting gas in each pixel and is obtained by integrating velocity-weighted flux, normalized to the total flux:

$$M_1 = \frac{\int_{v_i}^{v_f} v S_v dv}{\int_{v_i}^{v_f} S_v dv} \tag{2.2}$$

For the realization of both Moment 0 and Moment 1 images I have used CASA task `immoments` considering for the integration only pixels which had a flux ≥ 6 rms of the images of the datacube. From now on I will refer to rms as σ.

From the Moments 0, using the task `imstat`, I have obtained the flux density for each line within a region which contains source A. For most lines, this region consist of the 2 σ_M contour, where σ_M is the rms of the Moment 0 image obtained considering all the pixels (see Figure 2.2 and caption). But, for some lines, the emission resulted to come from a larger area presumably belonging to a common accretion cloud which surrounds both sources, so the 2 σ_M contour encloses both sources (see Figure 2.3). In this case, to consider only emission from source A, I calculated the flux density coming from the region enclosed by a higher value contour, i.e. a contour characterized by a value equal to a higher multiple of σ_M (read Tables 3.2, 3.3 and 3.6 captions). The flux density (S_{int}) is measured in $Jy \cdot km/s$ and the uncertainty on it, for each line, is assumed to be equal

to the square sum between the σ_M (converted in $Jy \cdot km/s$) of the respective Moment 0 image and the uncertainty on the flux calibration, which for this observation is 5% (Jørgensen et al. 2016):

$$\sigma_{S_{int}} = \sqrt{\sigma_M^2 + (0.05\ S_{int})^2} \tag{2.3}$$

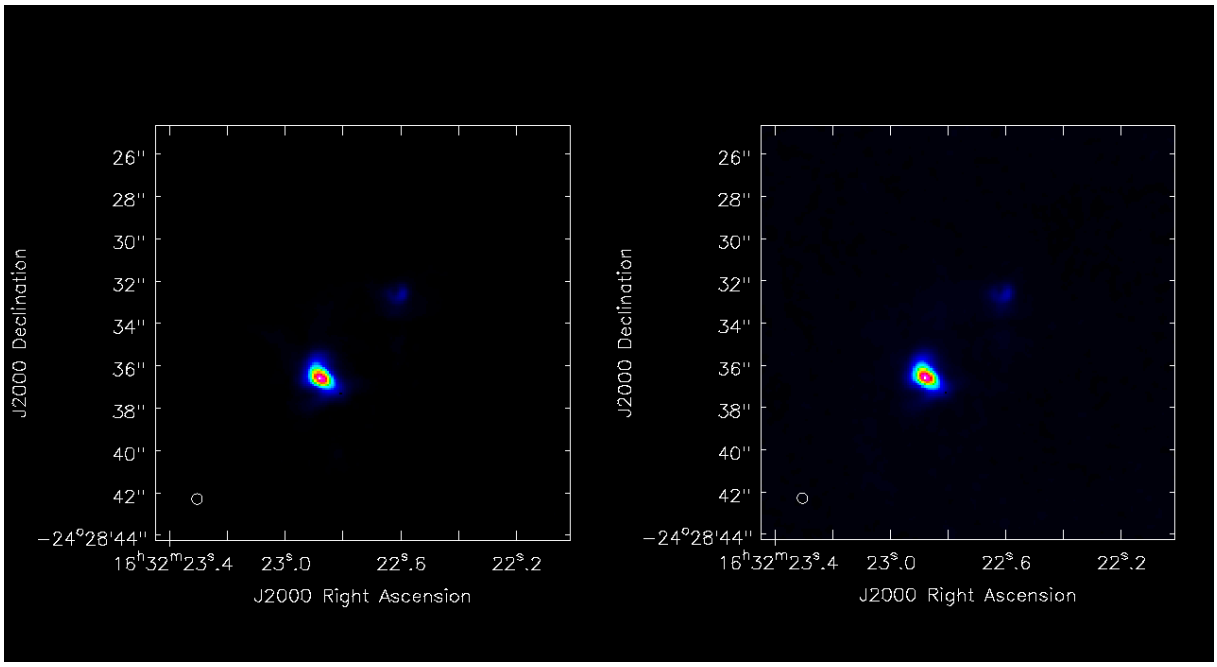

Figure 2.2: After excluding the lowest flux pixels from the integration, it makes no sense to calculate the rms for this resulting image because the background area selected would be featured by a zero or very low rms value (left image). The real contribution to the uncertainty on the measured flux densities is the rms of the Moment 0 image where the integration is made for all pixels (right image). The Moment 0 images in this figure are those realized for $C^{33}S$ $7-6$ transition.

Subsequently I have fitted these same contour regions of the Moment 0 maps with a gaussian function to get the position and its error of the peak for every line. The CASA task used for this purpose is `Gfit`. I have used it also to fit the continuum emission image (see Figure 2.4) to get the continuum peak position and refer each line peak position to it. The continuum source of this dataset is the one which is usually named as Aa submillimeter continuum source in literature. From now on on, when I talk about the continuum source, I will be referring to this source. The peaks distribution map is showed in the next chapter in Fig 3.13.

Moreover, for each transition I have considered the brightest pixel for source A from the Moment 0 images, extracted the spectra from there, and fitted the respective line with a gaussian. Same for the continuum peak pixel.

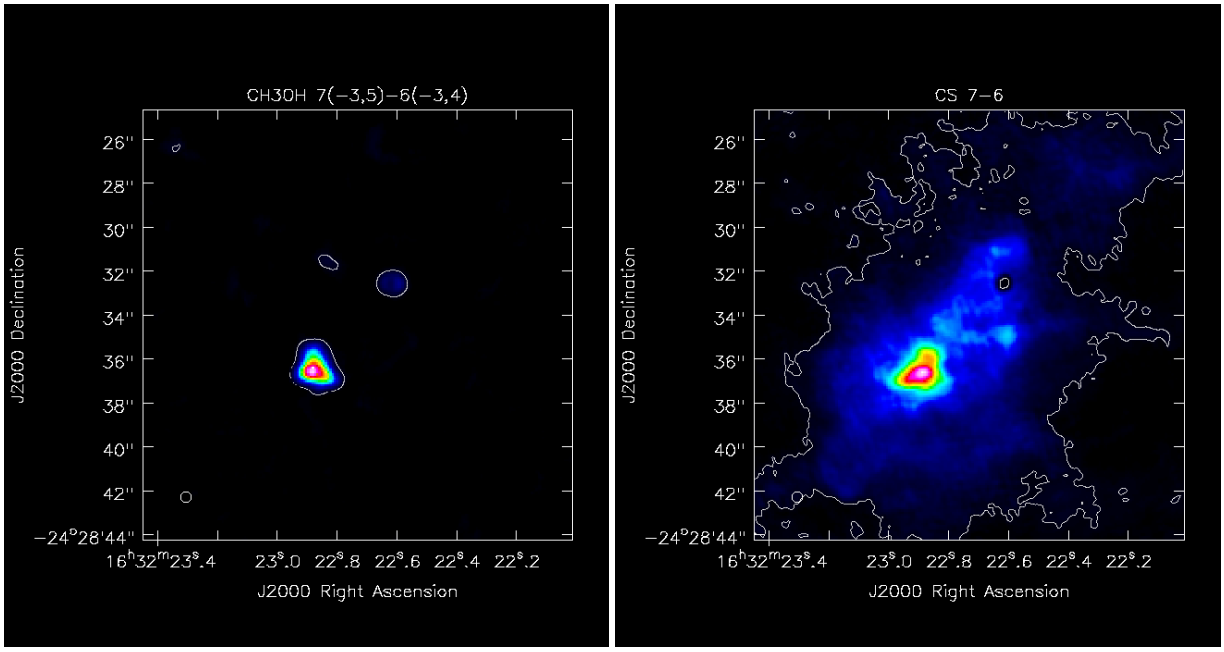

Figure 2.3: In this figure one can see the difference in the $2\sigma_M$ contours between a compact source such as CH_3OH (left image) and CS which emits from an extended area surrounding both sources (right image).

The datas obtained from this fits are shown in Tables 3.2, 3.3 and 3.6
For $^{13}CH_3OH$ transitions instead, I have fitted the lines in each pixel of the emitting region to get the gaussian area of every line for all the pixels to realize a rotational temperature and a total column density map of this species using rotational diagrams.

2.2.2 Rotational diagrams

According to Goldsmith et al. (1999) we know that the antenna theorem:

$$T_a = \frac{A_e}{2k} \int_{4\pi} B_\nu(\theta,\phi) P_n(\theta,\phi)\, d\Omega \tag{2.4}$$

under the assumption that

1. Our extended source emits uniformly over the beam

   becomes:

$$T_a = \left(\frac{\lambda^2}{2k}\right)\left(\frac{\Delta\Omega_s}{\Delta\Omega_a}\right) B_\nu \qquad , \tag{2.5}$$

   where the power pattern of the antenna is normalized so that $P_n(0,0) = 1$ and $\int_{4\pi} P_n(\theta,\phi)\, d\Omega = \Delta\Omega_a$ and I used the relation $A_e \Delta\Omega_a = \lambda^2$. A_e is the effective area

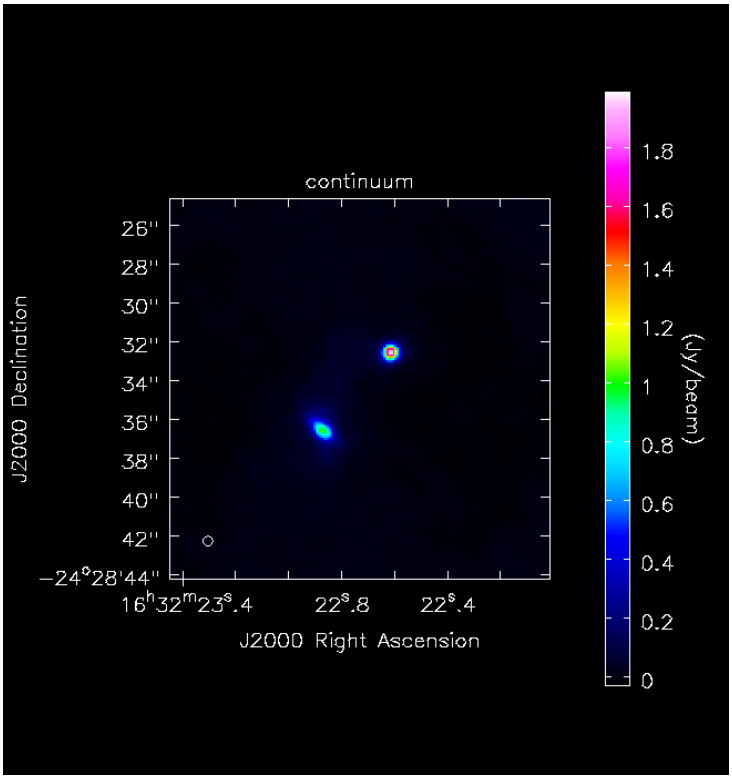

Figure 2.4: Continuum emission map of the PILS dataset

of the antenna, $\Delta\Omega_s$ is the source solid angle, $\Delta\Omega_a$ is the antenna solid angle (the beam).

Knowing that the brightness of a source at a temperature T and having optical depth τ is given by

$$B_\nu = \frac{\frac{h\nu}{k}}{e^{\frac{h\nu}{kT}} - 1} \left(\frac{1 - e^{-\tau}}{\tau} \right) \tau \tag{2.6}$$

and that the optical thickness of a transition u-l is

$$\tau = \frac{h}{\Delta\nu} N_u \frac{A_{ul} c^3}{8\pi h \nu^3} (e^{\frac{h\nu}{kT}} - 1) \tag{2.7}$$

we can rewrite 2.5:

$$N_u = \frac{8\pi k \nu^2 W}{h c^3 A_{ul}} \left(\frac{\Delta\Omega_a}{\Delta\Omega_s} \right) \left(\frac{\tau}{1 - e^{-\tau}} \right) \quad . \tag{2.8}$$

Where N_u is the column density of the upper state u, A_{ul} is the Einstein A-coefficient for the transition, Δv is the FWHM in units of velocity and I introduced the integral area of the line in $K\ km/s$:

$$W = \int T_a dv \approx T_a \Delta v \tag{2.9}$$

which can be thus approximated for a gaussian profile.

Making the following assumptions:

2. The source fills the beam ($\frac{\Delta\Omega_a}{\Delta\Omega_s} = 1$)
3. The emission is optically thin ($\tau << 1$)

the equation 2.8 becomes:

$$N_u^{thin} = \frac{8\pi k \nu^2 W}{hc^3 A_{ul}} \tag{2.10}$$

so I can get, for each pixel, the column density of a species in the state u simply by knowing the integral area, which I obtained from the gaussian fit, of the emission line corresponding to a transition u-l. Note that, because of assumption 1, the column density - and later the total column density and temperature - that I obtain for each pixel is the mean value over the beam area centered on that pixel.

In general, the probability for a system of being in a certain state j in relation to any other state i, i. e. the ratio of the column densities of the atoms/molecules in those states, follows the Boltzmann distribution:

$$\frac{N_u}{N_l} = \frac{g_u}{g_l} e^{-\frac{E_u - E_l}{T_{ex}}} \tag{2.11}$$

where N_u and N_l, g_u and g_l, E_u and E_l are respectively the column density, degeneracy level and the energy of states (in Kelvin) u and l. The excitation temperature T_{ex} of u-l transition is a physical quantity which depends on these parameters through this relation.

Assuming also that:

4. The source is at local thermal equilibrium (LTE)[1]

[1]The optical thickness of dust continuum implies a density of the colliders which is high enough to say that LTE is a good assumption for methanol. See Jørgensen et al. (2016) on this. By estimating line absorption from dust and the spectral index of its continuum emission, they deduced dust emission to be optically thick which allowed them to have a lower limit on dust column density. Thus, by knowing the gas-dust ratio and by making assumptions on the extent of the source (the observed 2D extension is also

T_{ex} will be the same for each transition i.e. T_{rot}, rotational temperature, since I am taking into account rotational transitions.

I am not making any assumption on the values of the collisional rates of the gas, but by assuming that the system is at LTE, I am saying that there are enough collisions to keep all the values of T_{ex} equal to the same value. In other words, if we are in a non-LTE condition and there is not a high collisional rate, there is a more frequent de-excitation of molecules. The higher the Einstein coefficient of a j-i transition is the more frequent it will be, resulting in a decrease of the $\frac{N_j}{N_i}$ ratio and, according to 2.11, of the T_{ex} of the transition. Thus, in non-LTE condition, the transitions with a higher Einstein coefficient will be the ones having a lower T_{ex}.

In our case, since all the T_{ex} are the same, from 2.11 I can write the column density of a species in the state u as a function of its rotational temperature and total column density:

$$N_u = \frac{N}{Z} g_u e^{-\frac{E_u}{T_{rot}}} \tag{2.12}$$

where Z is called partition function and it is equal to:

$$Z = \sum_j e^{-\frac{E_j}{T_{rot}}} \qquad . \tag{2.13}$$

In my analysis I obtained Z for $^{13}CH_3OH$ as a function of T_{rot} by interpolating values taken from the CDMS database[2]. See Figure 2.5.

We can rewrite 2.12:

$$\log \frac{N_u}{g_u} = -\frac{1}{T_{rot}} E_u + \log \frac{N}{Z} \tag{2.14}$$

so, by plotting $\log \frac{N_u}{g_u}$ vs E_u for different transitions of a certain species, with the assumptions we made being valid, we will have the points to be placed along a straight line. So I fitted the points with a straight line using Weighted Least Squares method and from this line's slope and intercept I obtained respectively T_{rot} and N. I estimated the uncertainties on the T_{rot} and N by considering the parameters which define straight line fits at the limit of acceptability (red dotted lines in Figure 2.6). These uncertainties are respectively of $\pm 30\ K$ and $\pm 5 \times 10^{14}\ cm^{-2}$.

the same along the line of sight direction), they estimated a lower limit for the density of the colliders of $n_{H_2} > 3 \times 10^{10}\ cm^{-3}$. This value have also been confirmed by comparing simulated methanol spectra and its observed lines. For n_{H_2} above this value, the excitations of methanol are determined by collisions

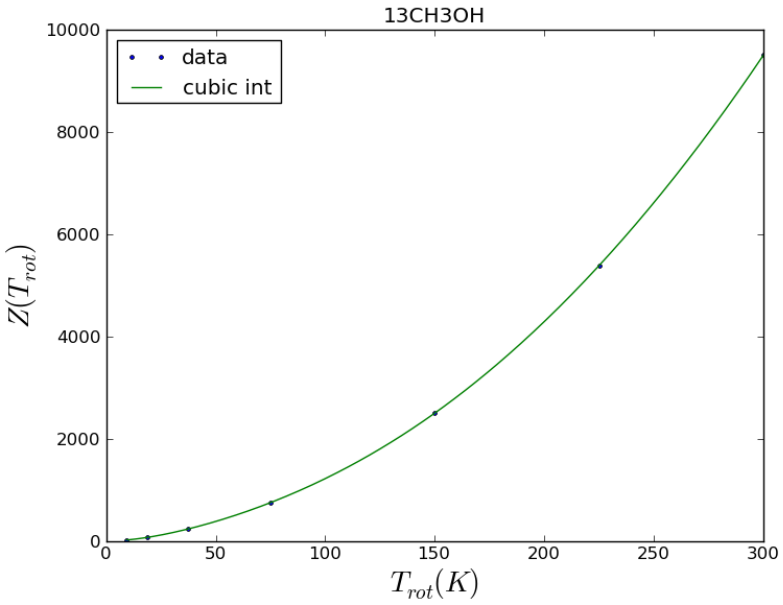

Figure 2.5: Interpolation of $^{13}CH_3OH$'s $Z(T_{rot})$ datas from CDMS database. I have interpolated using a cubic function.

Transitions	Gauss Area ($Jy\ beam^{-1}\ km\ s^{-1}$) CH_3OH	$^{13}CH_3OH$	Ratio
$7(1,6)-6(1,5)$	10.39 ± 0.27	3.92 ± 0.12	2.65 ± 0.11
$12(1,11)-12(0,12)$	8.15 ± 0.17	4.790 ± 0.075	1.702 ± 0.044
$13(1,12)-13(0,13)$	11.88 ± 0.22	5.043 ± 0.093	2.356 ± 0.062

Table 2.1: Methanol and ^{13}methanol lines' areas values and their ratios for different transitions. Values are obtained from the spectra extracted from the continuum peak pixel. Some of the transitions considered for methanol weren't possible to be considered also for ^{13}methanol because they were blended or too weak.

I wanted to apply this method to methanol (CH_3OH) lines to get its column density and rotational temperature in every pixel where its emission is observable. The problem is that the lines I was able to consider (i. e. bright enough and not blended) turned out the be optically thick: the $\frac{^{12}C}{^{13}C}$ ratio in ISM is estimated to be around 68 (Milam et al. 2005). In contrast line ratios between comparable methanol and ^{13}methanol lines suggest a ratio of unity, indicating that the main isotopologue is optically thick. See Table 2.1 for methanol and ^{13}methanol lines' integrated intensities and their ratios.

So I calculated the rotational diagram for ^{13}methanol considering the transitions listed

so LTE is a good assumption.

[2]http://www.astro.uni-koeln.de/cgi-bin/cdmsinfo?file=e033502.cat

Transitions	g_u	E_u (K)
$7(-1,7)-6(-1,6)$	15	69.01208
$7(0,7)-6(0,6)$	15	76.49883
$7(1,6)-6(1,5)$	15	84.49220
$11(0,11)-10(1,9)$	23	162.36265
$12(1,11)-12(0,12)$	25	192.65405
$13(1,12)-13(0,13)$	27	222.31547

Table 2.2: $^{13}CH_3OH$ transitions used for rotational diagrams with relative upper degeneracy and upper energy levels (taken from the CDMS database).

in Table 2.2. The idea is to get the total column density for each pixel for ^{13}methanol; methanol column densities can be obtained by multiplying these values by 68. Rotational temperature instead is the same for the two species. In Figure 2.6 is showed, as an example, the rotational diagram obtained for the continuum peak pixel. See Figures 3.2 and 3.3 in the next chapter for a map of the values obtained for every pixel.

The fact that no N_u values in Figure 2.6 show a significant drop from the trend of the straight line is consistent with the lines considered being optically thin. However it is not a proof that it is the case.

To have a proof I considered the total column density multiplied by 68 and temperature obtained from rotational diagram for ^{13}methanol in the continuum peak pixel and I used these values in RADEX simulator (Van der Tak et al. 2007) to obtain line emissions areas for methanol under these conditions. The output of the simulation shows[3] that there are some methanol lines which under these conditions are optically thin, such as $9(1,8)-8(-2,7)$ for e-methanol and $14(7,8)-15(6,9)$ for a-methanol:

- $9(1,8)-8(-2,7)$ is predicted to have an area of $104K\ km/s$ which is compatible with the measured value of $98K\ km/s$ keeping into account the magnitude of the uncertainty on the parameters obtained with rotational diagrams.
- $14(7,8)-15(6,9)$ is predicted to have an area of $141K\ km/s$ while I measure a value of $363K\ km/s$. But the explanation for measuring a value of around the double of the predicted one can be found in Figure 2.7: the line is blended with an other one of the same size. Thus, also in this case, the measured value is compatible with the predicted one.

The compatibility of these values shows that the assumption about ^{13}methanol optically thin lines is correct for the continuum pixel. And, since the total column density

[3]See Appendix A.

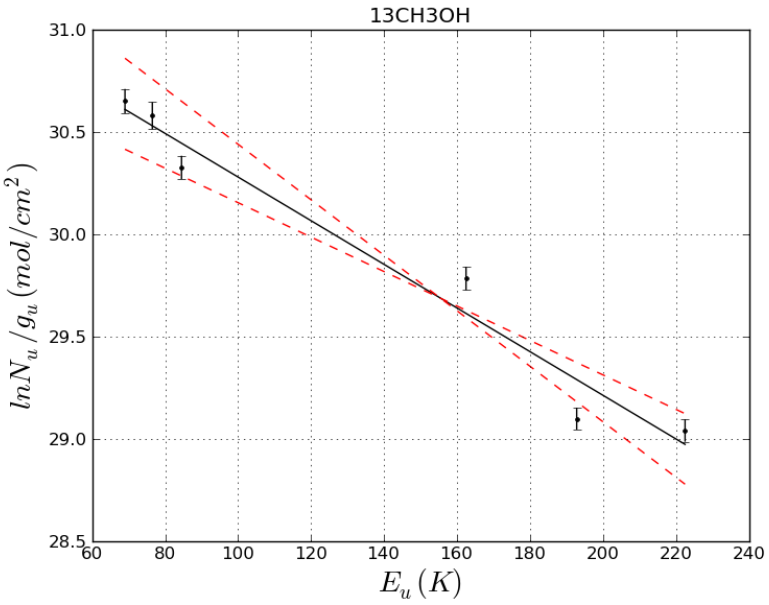

Figure 2.6: ^{13}methanol rotational diagram for the continuum peak pixel. The black continuous line is the best fit straight line. The red dotted lines indicate the limit fits within which the fit is acceptable.

increases toward the center, if some lines are optically thin in the continuum peak pixel they also will be for all the other pixels. So this proves that it was correct to use the rotational diagram method for every pixel.

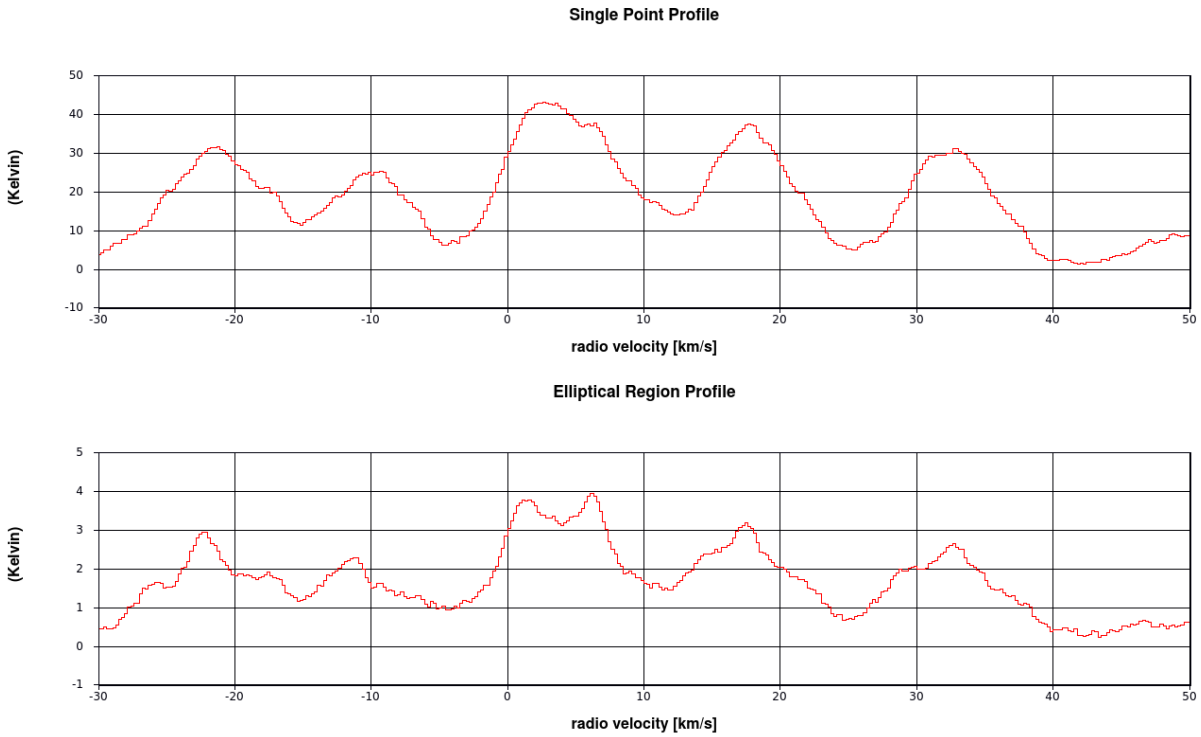

Figure 2.7: $14(7,8) - 15(6,9)$ measured area is twice as big as the predicted value because the line is blended with an other line of the same size. Upper image: spectrum extracted from the continuum pixel showing the line which I fitted to obtain its area. Lower image: spectrum extracted from an extended region enclosing the whole source A, showing that the line in the upper image is actually the result of the blending of two lines.

Chapter 3

Results and Discussions

3.1 Methanol and ^{13}methanol distribution and statistics

In this paragraph I am investigating the distribution of methanol and ^{13}methanol to obtain information about the extent of its emission region in order to understand how the heating from the central protostar influences the sublimation of methanol from the dust grains. Moreover, from its temperature distribution I plan to see if it shows a radial gradient (higher temperatures towards the center, lower in outer regions) or if there are other factors, e.g. outflows, which influence it.

In Figure 3.1 are shown the contours of Moment 0 images of all the methanol lines I have identified in this project. One should expect that the higher E_u transitions are emitting mostly from a compact region around the center of the source and the more we move far away from it the more important is the emission for increasingly lower E_u transitions. This is because we expect the gas temperature to decrease with the distance from the center (see §1.3.3). What we observe here instead is that all the contours from different transitions are remarkably the same - except for the $2(2,1) - 3(1,2)$ transition which presents slightly smaller contours - and that the FWHMs of all the 2D gaussian fits of the Moment 0 maps have a value of about 140×110 AU (deconvolved with the beam, see Table 3.1)[1]. This could mean that at the 20% contours most of the CH_3OH is frozen - that is why there is no more significant emission farther on - and that the temperatures of methanol for the pixels in the region enclosed inside these contours are very similar.

To investigate this I realized temperature and total column density maps of ^{13}methanol using rotational diagrams as I explained in the previous chapter. They are shown in Figures 3.2 and 3.3.

Figure 3.2 shows how rotational temperatures of ^{13}methanol - and thus of methanol - have values between 80 - 100 K which seem not to depend on the distance from the center.

[1]Another discussion on compact emission of methanol in this system has been done from Oya et al. (2016) but referring only to one transition.

Transitions	deconvolved FWHM (")
$2(2,1) - 3(1,2)$	maj.ax. 0.912 ± 0.060 min.ax. 0.575 ± 0.044
$7(1,6) - 6(1,5)$	1.152 ± 0.081 0.945 ± 0.068
$7(3,4) - 6(3,3)$	1.212 ± 0.092 0.951 ± 0.074
$7(-3,5) - 6(-3,4)$	1.157 ± 0.093 0.923 ± 0.077
$8(-3,6) - 9(-2,8)$	1.125 ± 0.095 0.763 ± 0.069
$11(1,10) - 11(0,11)$	1.208 ± 0.072 1.105 ± 0.066
$12(1,11) - 12(0,12)$	1.194 ± 0.074 1.024 ± 0.064
$13(1,12) - 13(0,13)$	1.107 ± 0.066 0.968 ± 0.059

Table 3.1: FWHMs of the 2D gaussian fits of deconvolved Moment 0 maps for all methanol emission lines

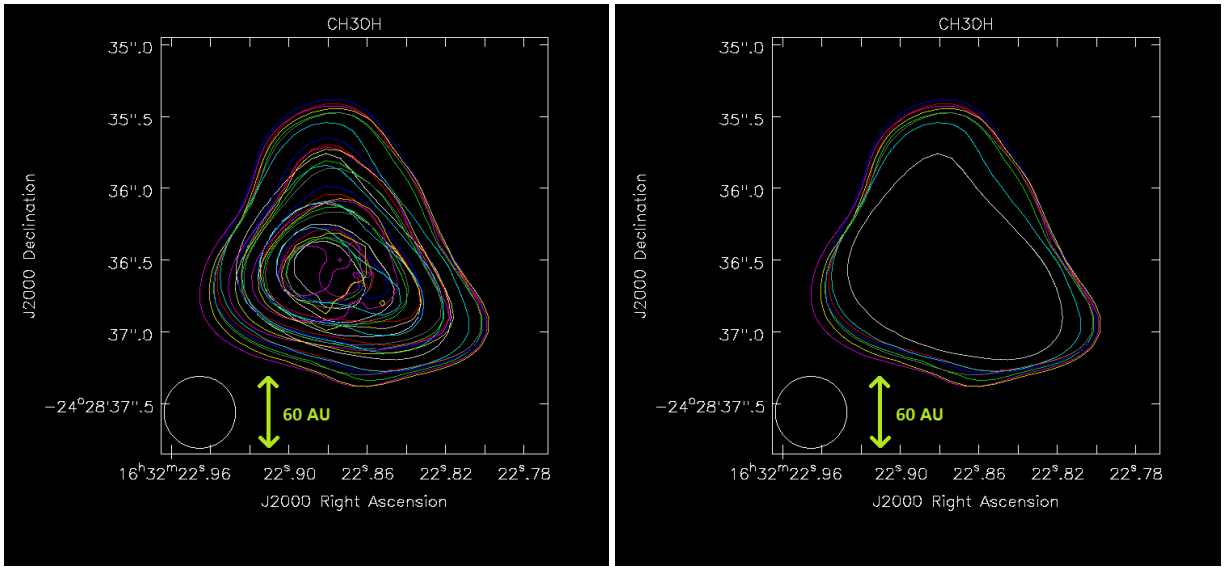

Figure 3.1: Left image: 80%, 60%, 40% and 20% of the peak value contours. Right image: 20% of the peak value contours. Methanol transitions considered are:
White: $2(2,1) - 3(1,2)$, $E_u = 44.67212\ K$
Green: $7(1,6) - 6(1,5)$, $E_u = 80.09107\ K$
Blue: $7(3,4) - 6(3,3)$, $E_u = 112.70871\ K$
Red: $7(-3,5) - 6(-3,4)$, $E_u = 127.70675\ K$
Cyan: $8(-3,6) - 9(-2,8)$, $E_u = 146.27399\ K$
Magenta: $11(1,10) - 11(0,11)$, $E_u = 169.00745\ K$
Yellow: $12(1,11) - 12(0,12)$, $E_u = 197.07334\ K$
Gray: $13(1,12) - 13(0,13)$, $E_u = 227.47254\ K$

But it is evident that there are two regions in which I measured higher temperatures. These warmer regions are compatible with regions crossed by an East-West outflow which has been previously detected for this system (see Figure 3.4 from Loinard et al. 2013).

This suggests that this gas is heated by shocks due to the outflow. Moreover it could also explain the horizontally elongated structure at the bottom of the emitting region since shocks are able to destroy grain mantles (see §1.3.4) and release methanol molecules in the gas phase.
However, this is not the only possible explanation for this structure: it is also plausible that the elongation simply traces the disk structure. In fact for grains belonging to the disk, even at distances from the protostar where grains' temperatures aren't high enough to allow methanol to reach its sublimation point, there can be release of methanol in the gas phase due to grain-grain collisions. To look into this possibility, I plotted together continuum emission (which represents emission from the disk) contours with a contour of a methanol transition. From Figure 3.5 one can clearly notice that continuum emission shape doesn't follow the horizontally elongated structure of methanol emission, so its release in the gas phase is probably not due to grain-grain collisions.

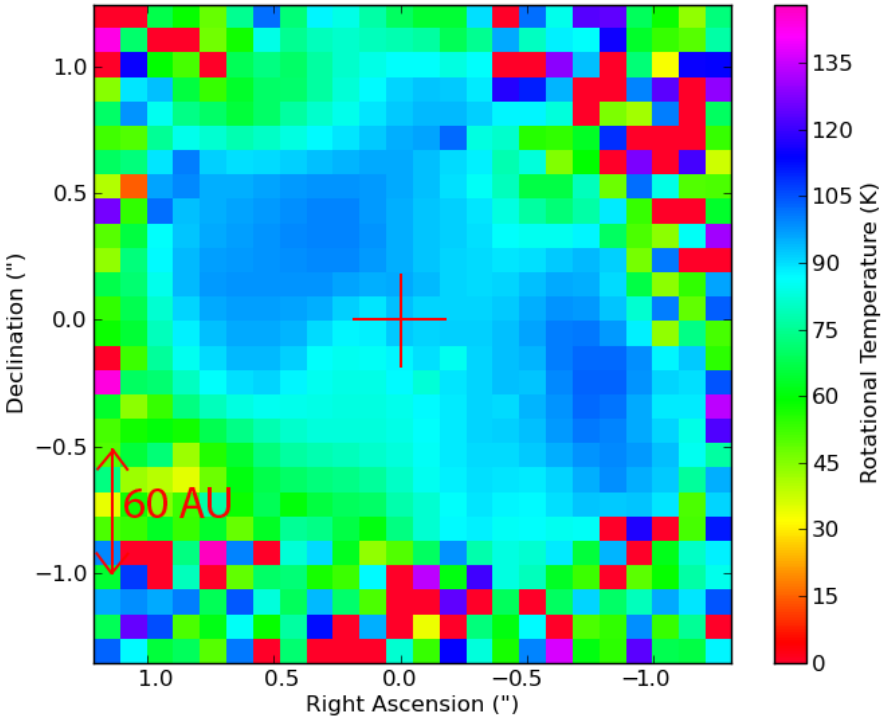

Figure 3.2: ^{13}methanol rotational temperature map. The coordinates are referred to the continuum peak position (indicated with the red cross).

To examine the first hypothesis, I extracted the mean spectra from the two warm regions, and it turned out that all methanol lines are blueshifted in the western warm region and redshifted in the eastern warm region, a characteristic that doesn't occur for any of the other species' lines. This is displayed in Figure 3.6 for $12(1,11) - 12(0,12)$ transition. This could be an evidence that these areas are interested by shocks.

The most plausible scenario is therefore that shocks due to an East-West outflow heat up the methanol in the gas phase they sweep up, and that these same shocks cause sputtering of dust grains and consequent release of methanol in the gas phase along the E-W direction. So we observe this horizontally elongated structure for methanol emission.

In general, as it is shown in Moment 0 maps in Figures 3.7, 3.9 and 3.10, the ^{13}methanol and methanol emission is compact and concentrated around the continuum source although there is also a weak emission from the envelope. All Moment 1 maps (Figures 3.8, 3.11 and 3.12) show a velocity gradient perpendicular to the North East - South West

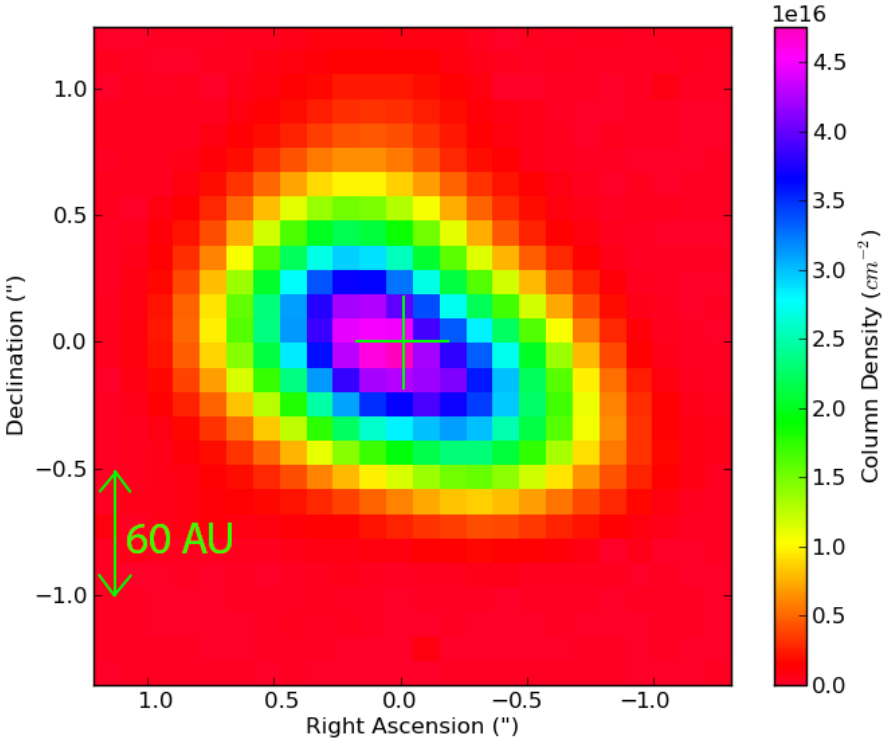

Figure 3.3: ^{13}methanol total column density map. The coordinates are referred to the continuum peak position (indicated with the green cross).

outflow (also mentioned in Loinard et al. 2013 and discussed here in §3.2). Moreover, some methanol Moment 1 images show high velocities toward the SW part of the image. See discussion on velocity distribution in §3.2.

In Tables 3.2 and 3.3 are presented the statistics of the gaussian fits of all ^{13}methanol and methanol lines examined in this project for the brightest pixel for that transition and for the continuum peak pixel.

Transitions	Frequency lit. (GHz)		V_0 ($km\ s^{-1}$)	σ_{V_0}	FWHM ($km\ s^{-1}$)	σ_{FWHM}	Int ($Jy\ beam^{-1} km\ s^{-1}$)	σ_{Int}	S_{int} ($Jy\ km\ s^{-1}$)	$\sigma_{S_{int}}$
$7(-1,7)-6(-1,6)$	330.19404	cont.px. br.px.	4.127 3.207	0.059 0.086	7.61 7.71	0.15 0.22	5.26 5.38	0.13 0.20	14.84	0.74
$7(0,7)-6(0,6)$	330.00175		3.86	0.12	8.56	0.30	5.20	0.23	12.75	0.64
$7(1,6)-6(1,5)$	330.44242		3.414 2.470	0.063 0.064	6.58 6.22	0.15 0.15	3.92 4.01	0.12 0.13	11.80	0.59
$11(0,11)-10(1,9)$	348.10019		3.272 0.966	0.037 0.023	5.002 3.627	0.087 0.056	2.509 2.658	0.058 0.053	6.82	0.34
$12(1,11)-12(0,12)$	335.56021		3.352	0.032	6.423	0.076	4.790	0.075	12.69	0.63
$13(1,12)-13(0,13)$	341.13166		3.274	0.040	6.804	0.095	5.043	0.093	13.48	0.67

Table 3.2: Statistics obtained from gaussian fits of the ^{13}methanol I examined. Uncertainties on flux densities (S_{int}) are given by 2.3. V_0 = Gauss Center, Int = Gauss Area. cont.px. = continuum peak pixel, br.px. = brightest pixel. Where the results of only one fit are reported, it means that the continuum peak pixel and the brightest pixel coincide.

Transitions	Frequency lit. (GHz)		V_0 ($km\ s^{-1}$)	σ_{V_0}	FWHM ($km\ s^{-1}$)	σ_{FWHM}	Int ($Jy\ beam^{-1} km\ s^{-1}$)	σ_{Int}	S_{int} ($Jy\ km\ s^{-1}$)	$\sigma_{S_{int}}$
$2(2,1)-3(1,2)$	335.13369	cont.px. br.px.	2.785 3.378	0.066 0.059	8.83 9.44	0.17 0.15	7.78 8.28	0.19 0.17	23.7	1.2
$7(-3,5)-6(-3,4)$	338.55993		3.002 1.631	0.047 0.053	7.59 6.49	0.11 0.13	7.74 8.00	0.15 0.21	39.0	1.9
$7(1,6)-6(1,5)$	341.41564		3.680 2.905	0.078 0.098	9.64 9.35	0.20 0.24	10.39 11.34	0.27 0.38	49.5[a]	2.5
$7(3,4)-6(3,3)$	338.58319		3.520 1.932	0.037 0.049	7.614 6.67	0.088 0.12	7.78 8.21	0.12 0.19	42.6	2.1
$8(-3,6)-9(-2,8)$	330.79391		2.957 1.386	0.040 0.042	6.741 5.31	0.095 0.10	5.52 5.79	0.10 0.15	24.7	1.2
$11(1,10)-11(0,11)$	331.50237		3.395 2.093	0.055 0.061	8.90 7.21	0.14 0.14	9.68 9.52	0.19 0.25	50.8	2.5
$12(1,11)-12(0,12)$	336.86511		2.934 3.492	0.051 0.052	7.52 8.30	0.12 0.12	8.15 9.39	0.17 0.18	49.0	2.5
$13(1,12)-13(0,13)$	342.72983		2.888 2.236	0.059 0.065	9.90 9.26	0.14 0.15	11.88 12.10	0.22 0.26	59.7[a]	3.0

Table 3.3: Statistics obtained from gaussian fits of the methanol I examined. Uncertainties on flux densities (S_{int}) are given by 2.3. V_0 = Gauss Center, Int = Gauss Area. cont.px. = continuum peak pixel, br.px. = brightest pixel.
a: Flux density calculated inside a 3.5σ contour. See §2.2.1.

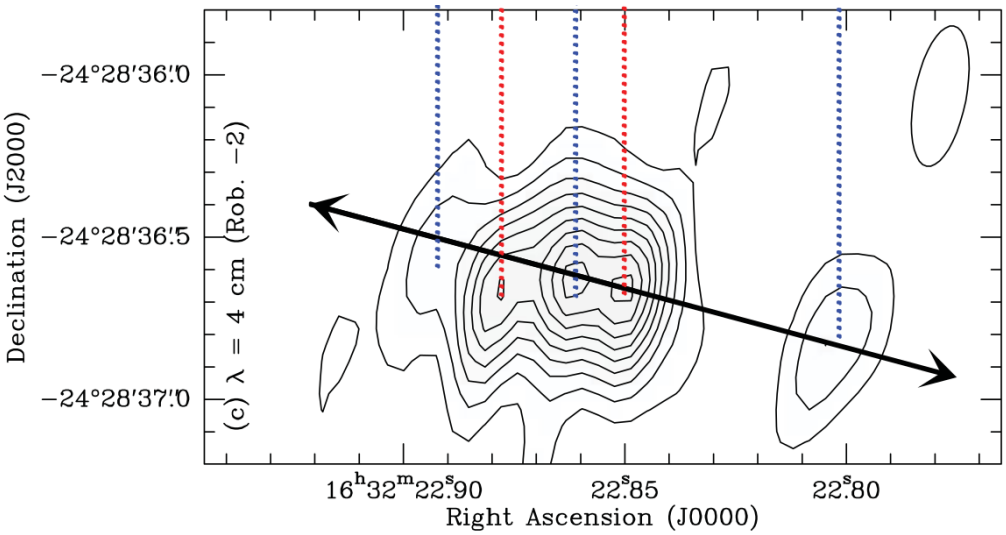

Figure 3.4: 4 cm VLA continuum image from Loinard et al. (2013). The black arrows indicate the direction of the outflows. The dotted red lines point are the centimeter continuum sources while the blue ones denote the ejecta.

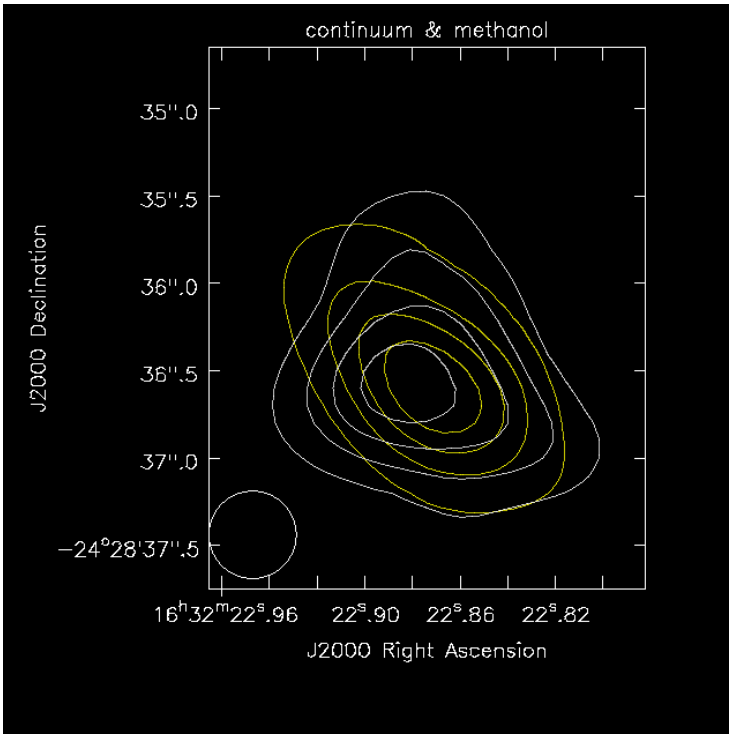

Figure 3.5: 80%, 60%, 40% and 20% of the peak value contours for continuum emission (yellow) and $11(1,10)-11(0,11)$ methanol transition (white). It is clear that continuum emission shape doesn't follow the horizontally elongated structure of methanol emission.

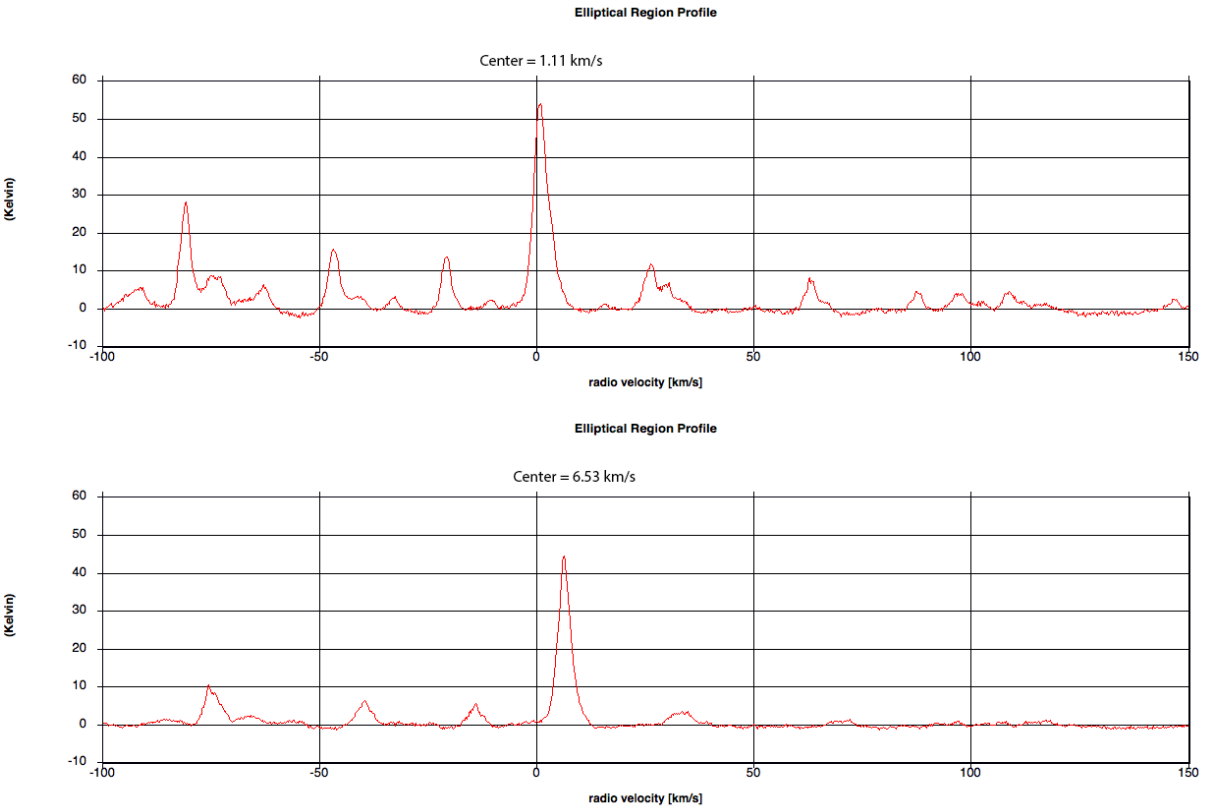

Figure 3.6: Mean spectra extracted from the western warm region (upper image) and from the eastern one (lower image) presenting respectively the blueshifted and the redshifted $12(1,11)-12(0,12)$ methanol line. Note also that the blueshifted line is more intense than the redshifted one.

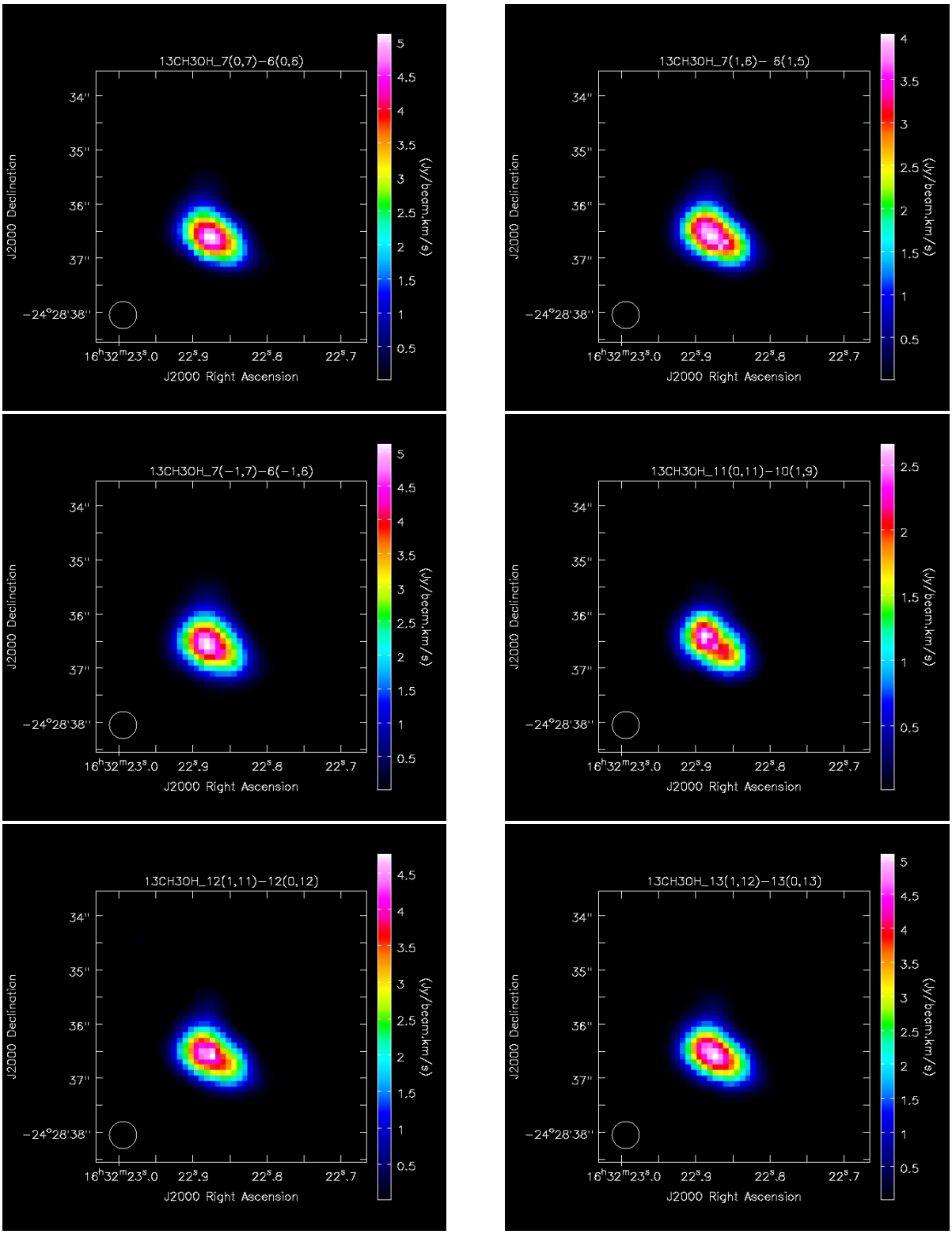

Figure 3.7: Moment 0 maps of Source A for ^{13}methanol emission lines.

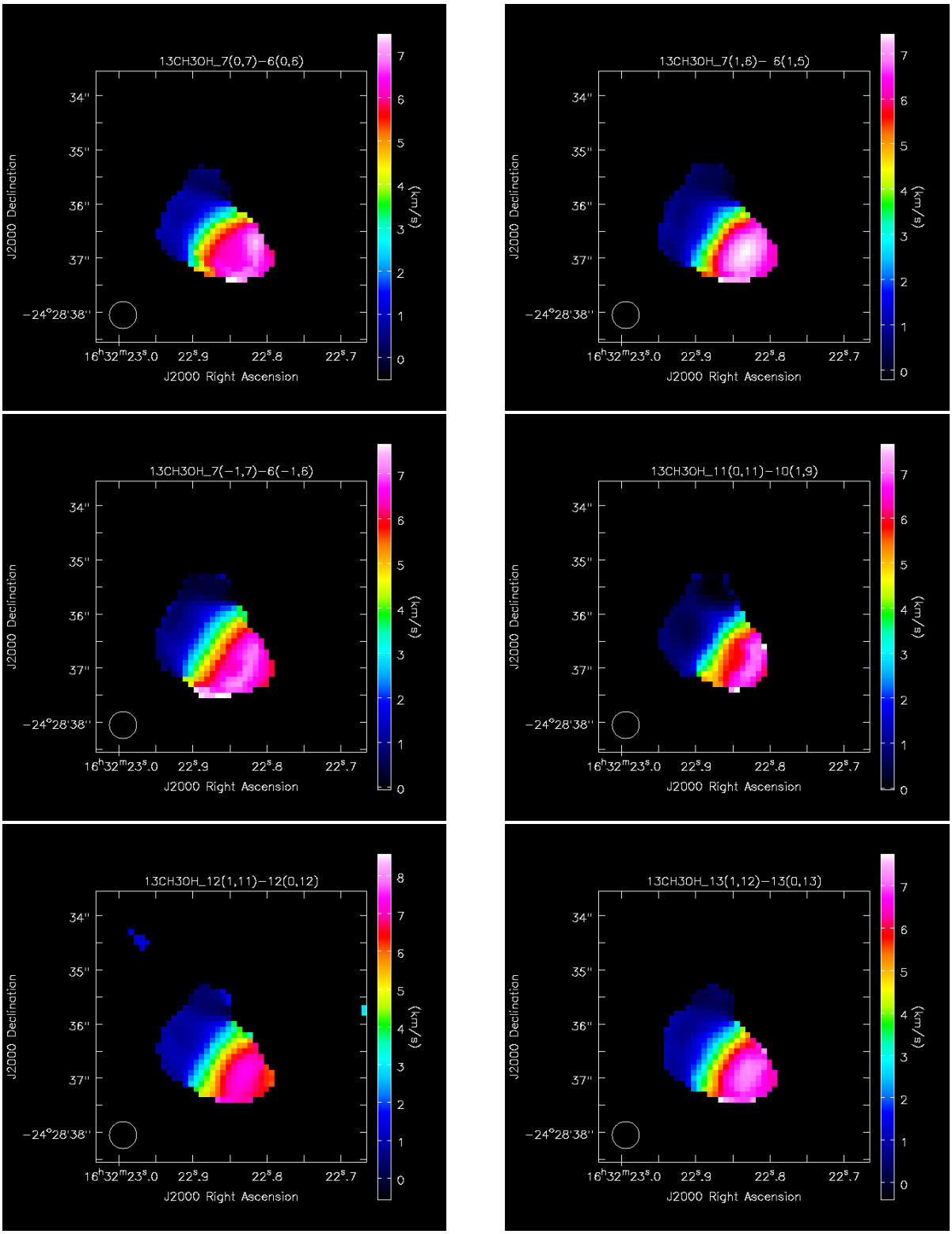

Figure 3.8: Moment 1 maps of Source A for ^{13}methanol emission lines.

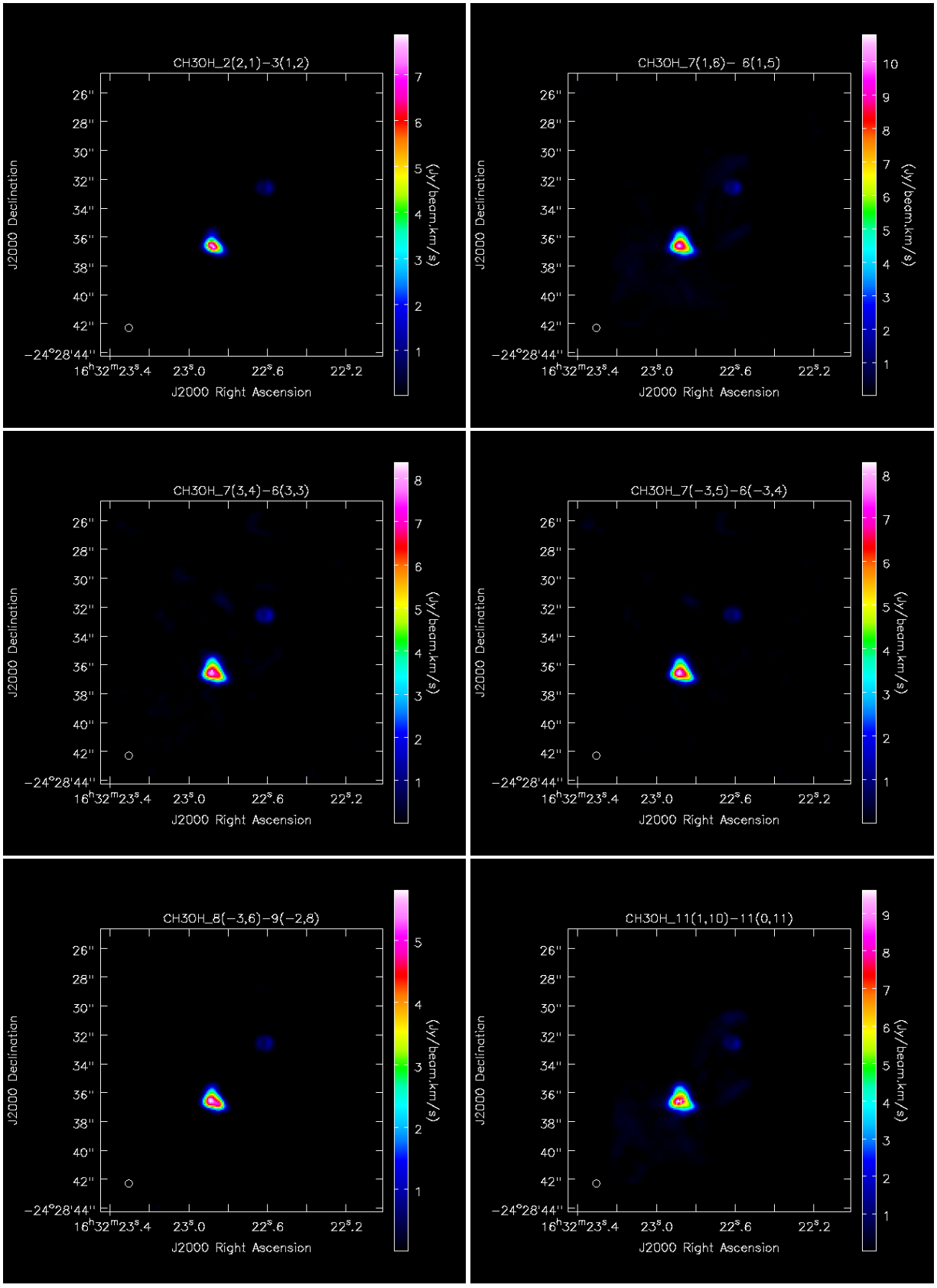

Figure 3.9: Moment 0 maps for methanol emission lines. 1 of 2.

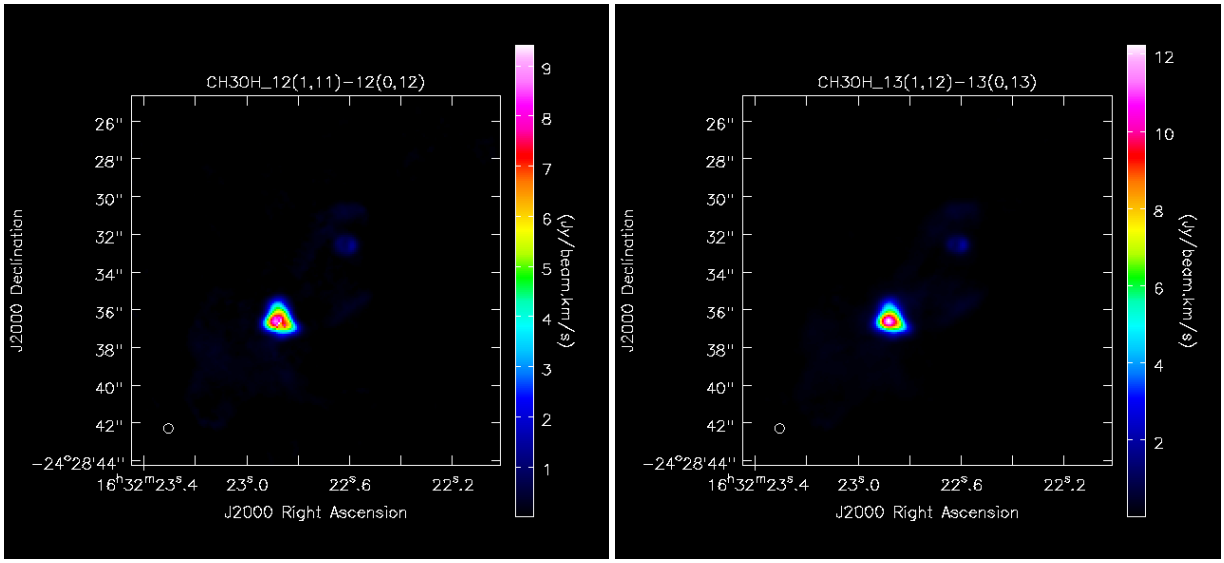

Figure 3.10: Moment 0 maps for methanol emission lines. 2 of 2.

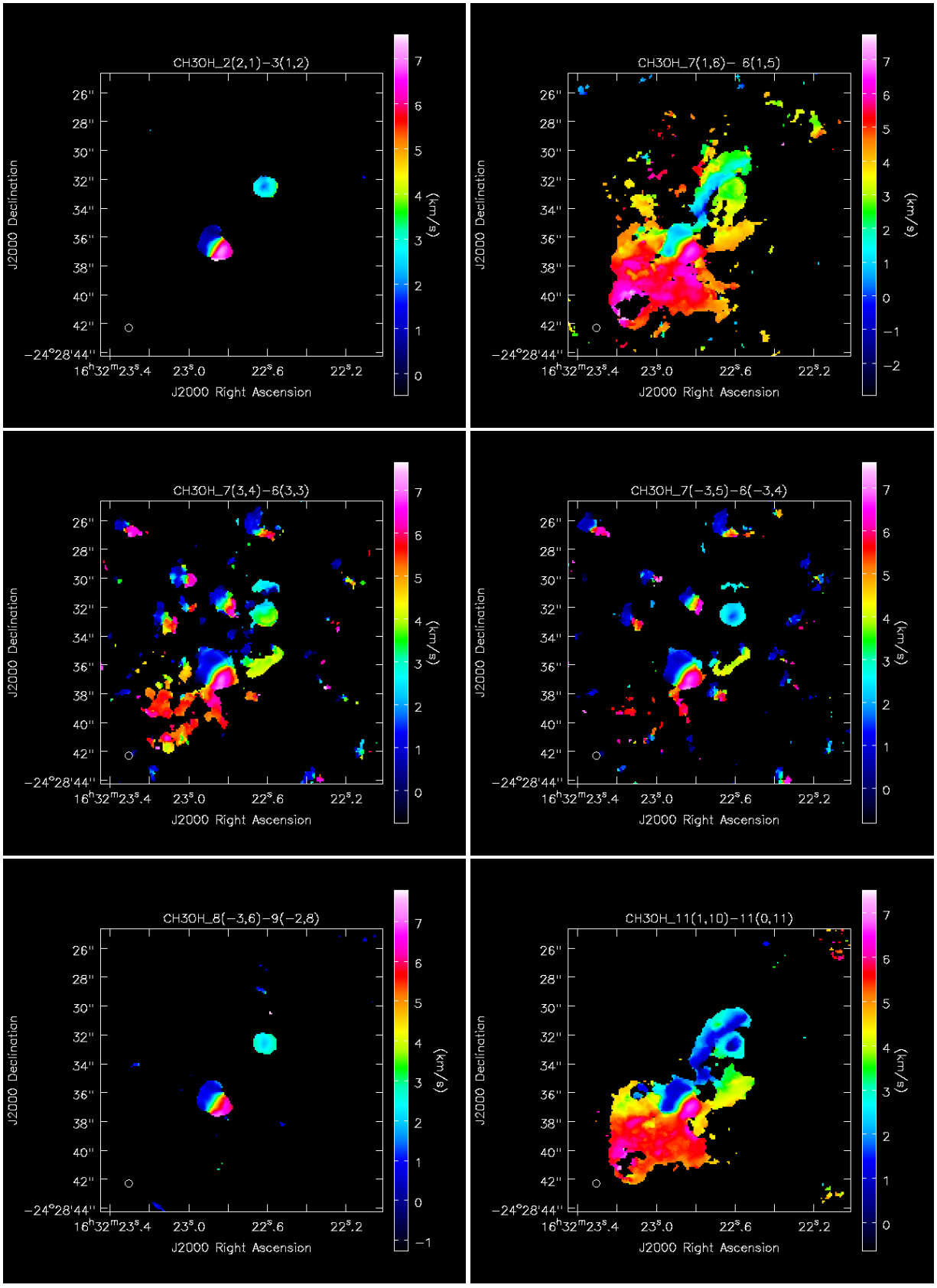

Figure 3.11: Moment 1 maps for methanol emission lines. 1 of 2.

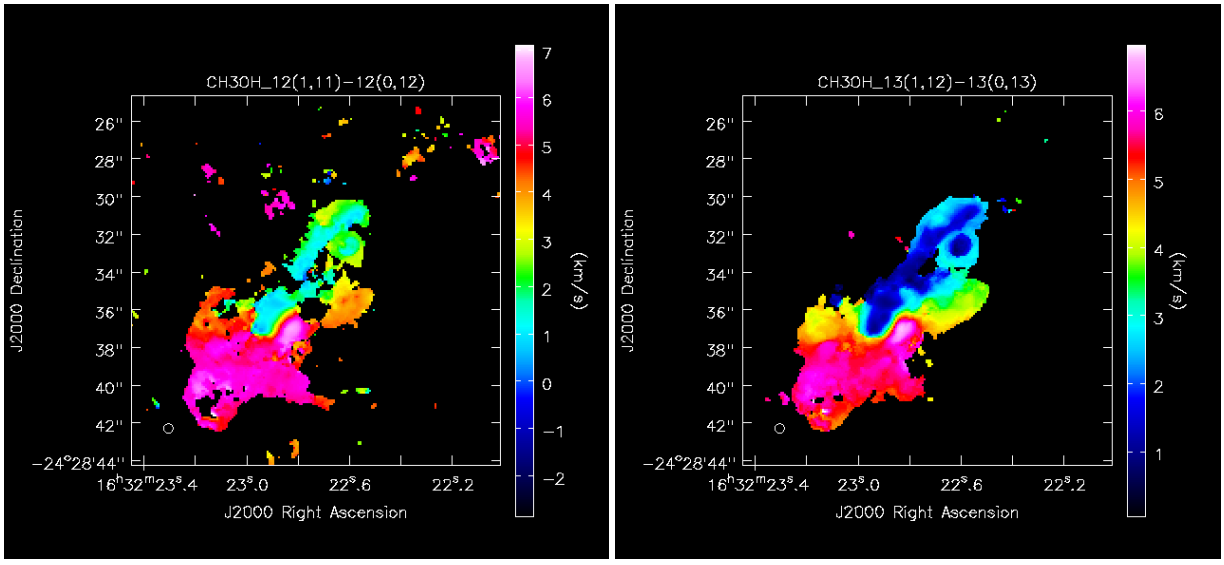

Figure 3.12: Moment 1 maps for methanol emission lines. 2 of 2.

3.2 Other species distribution and statistics

Here I investigate the distribution of different species to understand if they are located towards the hot corino or the envelope (or both) of the system. Moreover, it is interesting to map the peaks positions for the various transitions, in order to evidence eventual peculiarities in their distribution; for example to see if they are all distributed close to the disk or if some of them are located far from it because of the influence of outflows.

The positions of the peaks of different emission lines and their relative uncertainties obtained from fitting Moment 0 maps are plotted in Figure 3.13 and listed in Tables 3.4 and 3.5. The statistics for these lines can be found in 3.6. For the map I considered only one methanol transition since ^{13}methanol and methanol lines peak remarkably all in the same area.
As said in §1.3.4, SiO can be used as a tracer of outflows since it is formed by reaction between OH or H_2 and silicon present in the gas-phase after being released from dust grains due to shocks. From its Moment 0 map in Figure 3.14 it can be seen how its emission is an evidence of the presence of the North East - South West outflow. That is also the reason why its peak is located so far away from the continuum peak compared to the other transitions. What is interesting to notice by looking at the peaks map is that most of the peaks are not exactly located around the continuum peak but there is an offset towards South West. This suggests that these species are influenced by the action of the NE-SW outflow. In particular, $SO\ \ 3\Sigma\ \ 7(8)-6(7)$ peaks also considerably far away from the center, and its integrated emission is elongated along the NE-SW direction, same as SiO, while $SO\ \ 3\Sigma\ \ 3(3)-3(2)$ doesn't show this peculiarity (see Figure 3.15). Moreover, by looking at $SO\ \ 3\Sigma\ \ 7(8)-6(7)$ and $SiO\ \ 8-7$ Moment 1 maps in Figure 3.16, it is clear that they feature similar velocity distributions. A possible explanation for these features is that $SO\ \ 3\Sigma\ \ 7(8)-6(7)$ transition, which has a higher E_u than $SO\ \ 3\Sigma\ \ 3(3)-3(2)$, is enhanced in the regions crossed by the NE-SW outflow because shocks heat the gas, allowing more SO molecules to reach the 7(8) excited state. From Figure 3.13 also note that $C^{17}O\ \ 3-2$ and $HCS+\ \ 8-7$ transitions don't show the above-mentioned offset.

Moment 0 maps show also that all other transitions' emission is mainly located towards the disk, which is identified by the continuum emission, even if some species such as CO, CS, H_2CO and, less intensely, H_2CS and $H^{13}CN$ also present emission from the envelope (see Figure 3.17). This contrasts with Figure 1.9 from §1.4 which summarizes single dish and interferometer observations from 2011, in fact species such as CS, H_2CS and HCN[2] are there reported as belonging only to Source A, while from the Moment maps I realized they show emission also from the envelope. Also SO is reported to emit only around Source A but, as aforesaid, it is influenced by NE-SW outflow which causes its emission to extend towards the envelope.

[2]I realized the map for $H^{13}CN$ which, even being less abundant than HCN (being its isotopologue), shows some emission from the envelope. This implies that also HCN emits significantly from the envelope.

Species & Transitions	J2000 Peaks Positions
$^{34}SO \;\; 9(8) - 8(7)$	RA 16:32:22.87609 ± 0.00072 DEC -024.28.36.56378 ± 0.01156
$C^{17}O \;\; 3 - 2$	16:32:22.8767 ± 0.0042 -024.28.36.4935 ± 0.0856
$SiO \;\; 8 - 7$	16:32:22.946 ± 0.019 -024.28.37.281 ± 0.202
$H_2CO \;\; 5(1,5) - 4(1,4)$	16:32:22.8866 ± 0.0046 -024.28.36.5920 ± 0.0529
$SO_2 \;\; 14(4,10) - 14(3,11)$	16:32:22.87739 ± 0.00102 -024.28.36.64844 ± 0.01553
$C^{33}S \;\; 7 - 6$	16:32:22.8768 ± 0.0013 -024.28.36.5413 ± 0.0181
$H_2CS \;\; 10(1,9) - 9(1,8)$	16:32:22.8748 ± 0.0019 -024.28.36.5605 ± 0.0267
$SO_2 \;\; 24(2,22) - 23(3,21)$	16:32:22.87482 ± 0.00108 -024.28.36.59800 ± 0.01721
$C_{34}S \;\; 7 - 6$	16:32:22.8786 ± 0.0023 -024.28.36.5533 ± 0.0350
$SO_2 \;\; 5(3,3) - 4(2,2)$	16:32:22.8785 ± 0.0014 -024.28.36.6152 ± 0.0209
$HCS+ \;\; 8 - 7$	16:32:22.8690 ± 0.0034 -024.28.36.5172 ± 0.0535
$SO \;\; 3\Sigma \;\; 3(3) - 3(2)$	16:32:22.8745 ± 0.0013 -024.28.36.6125 ± 0.0203
$CH_3OH \;\; 7(1,6) - 6(1,5)$	16:32:22.8745 ± 0.0021 -024.28.36.5444 ± 0.0284

Table 3.4: Peaks positions and relative uncertainties. Right Ascensions are expressed in hours:minutes:seconds, Declinations in degrees.arcmins.arcsecs. 1 of 2

Species & Transitions	J2000 Peaks Positions
$HDCO \;\; 5(1,4) - 4(1,3)$	16:32:22.8759 ± 0.0014 -024.28.36.5536 ± 0.0191
$SO \;\; 3\Sigma \;\; 7(8) - 6(7)$	16:32:22.8885 ± 0.0036 -024.28.36.7562 ± 0.0494
$CS \;\; 7 - 6$	16:32:22.8924 ± 0.0043 -024.28.36.6042 ± 0.0539
$OCS \;\; 29 - 28$	16:32:22.8799 ± 0.0015 -024.28.36.5735 ± 0.0246
$H^{13}CN \;\; 4 - 3$	16:32:22.8824 ± 0.0016 -024.28.36.6121 ± 0.0243
Continuum	16:32:22.8733 ± 0.0020 -024.28.36.5454 ± 0.0298

Table 3.5: Peaks positions and relative uncertainties. Right Ascensions are expressed in hours:minutes:seconds, Declinations in degrees.arcmins.arcsecs. 2 of 2

Moment 0 maps of other transitions are shown in Figures 3.18 and 3.19.

Moment 1 maps in Figure 3.20, 3.21 and 3.22 show that all the species present, toward Source A, a velocity gradient perpendicular to the NE-SW outflow. This means that they might all belong to the same gas cloud, rotating around the protostar. Moreover, from Moment 1 maps, for the species observed also in the envelope, it is possible to appreciate that the effect of the NE-SW outflow on these species reveals also in the velocity distribution (besides the above-mentioned effect on peak distribution). These Moment 1 maps, in Figure 3.20, in fact show a velocity pattern which, to some extent, resembles the ones from $SO\ \ 3\Sigma\ \ 7(8)-6(7)$ and $SiO\ \ 8-7$, with high velocities toward SW part of the image. This applies also to some methanol Moment 1 images, as mentioned in the previous paragraph, suggesting that methanol is also influenced by the NE-SW outflow.

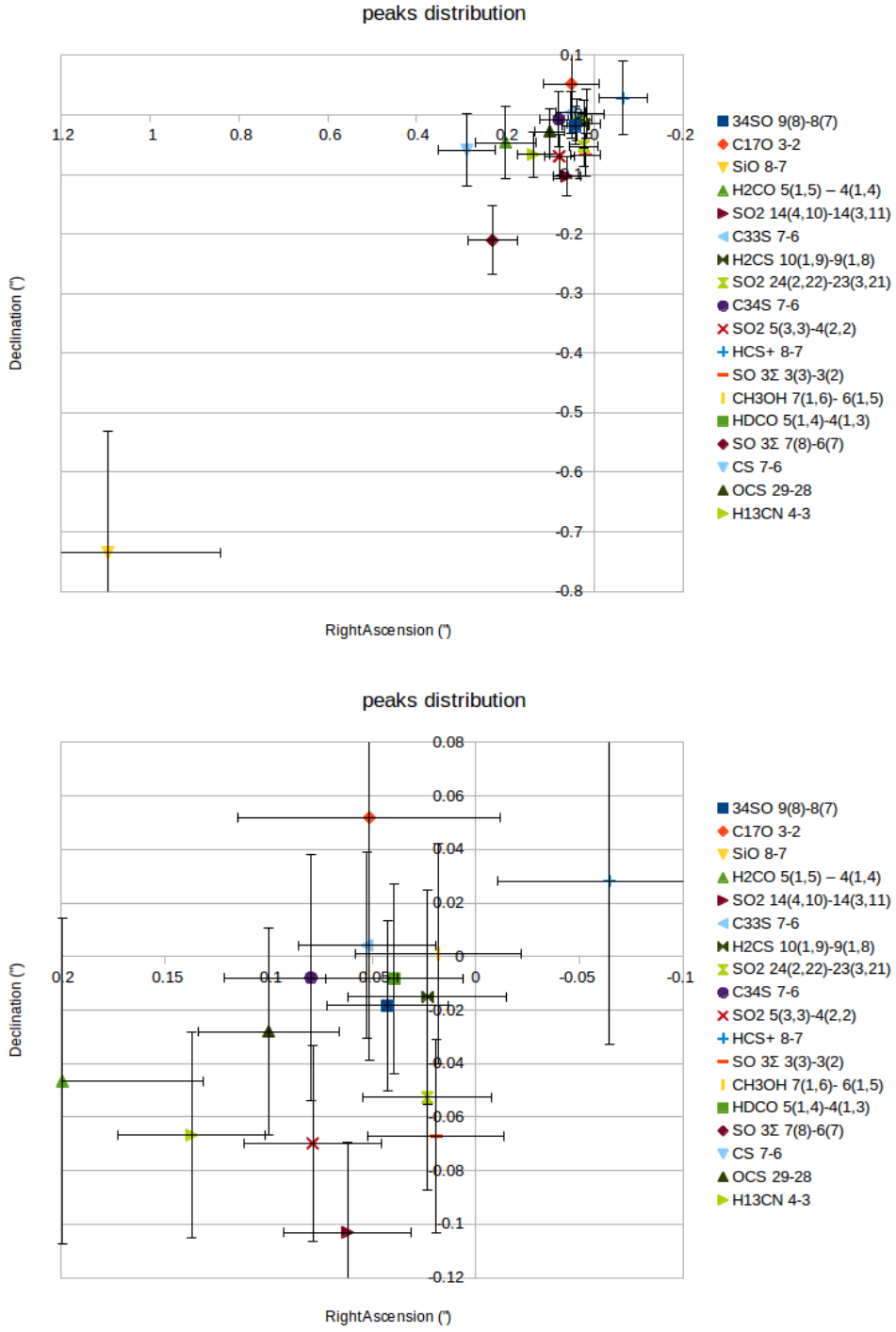

Figure 3.13: Peaks distribution map. All the positions are referred to the continuum peak position. In the lower image there is a zoom on the area close to the continuum peak.

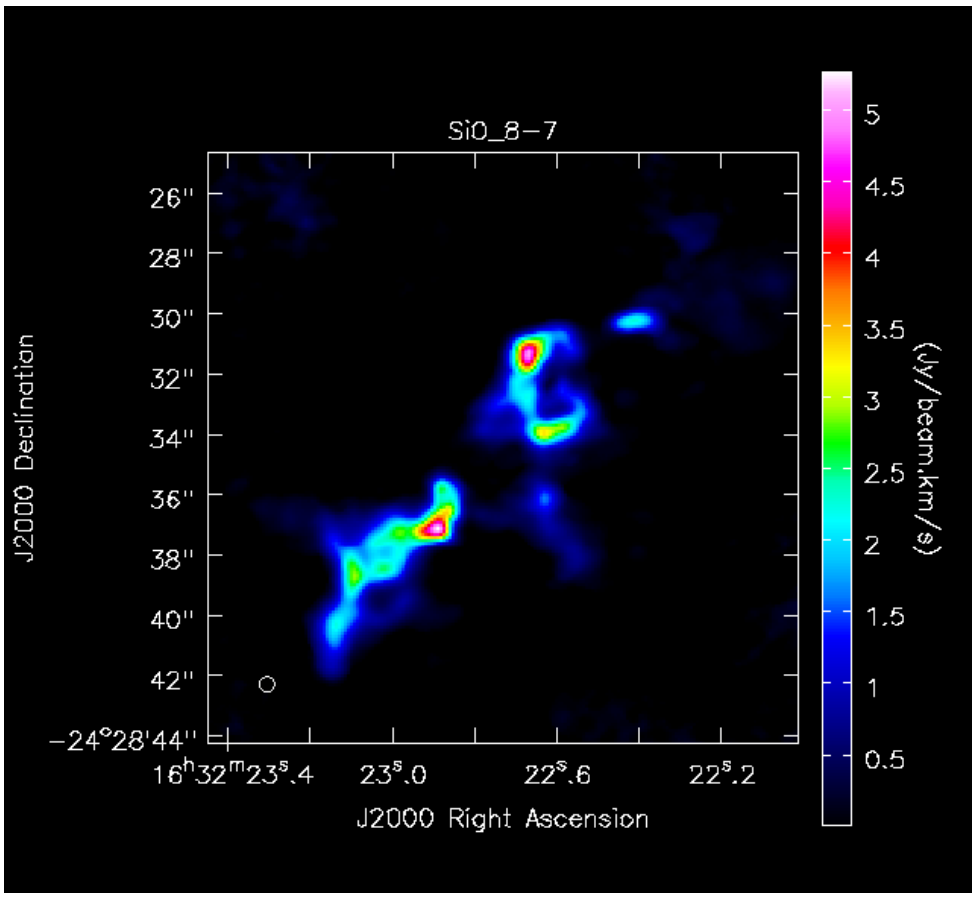

Figure 3.14: *SiO* $8-7$ Moment 0 map. Its North East - South West elongated structure suggests the presence of an outflow along that direction.

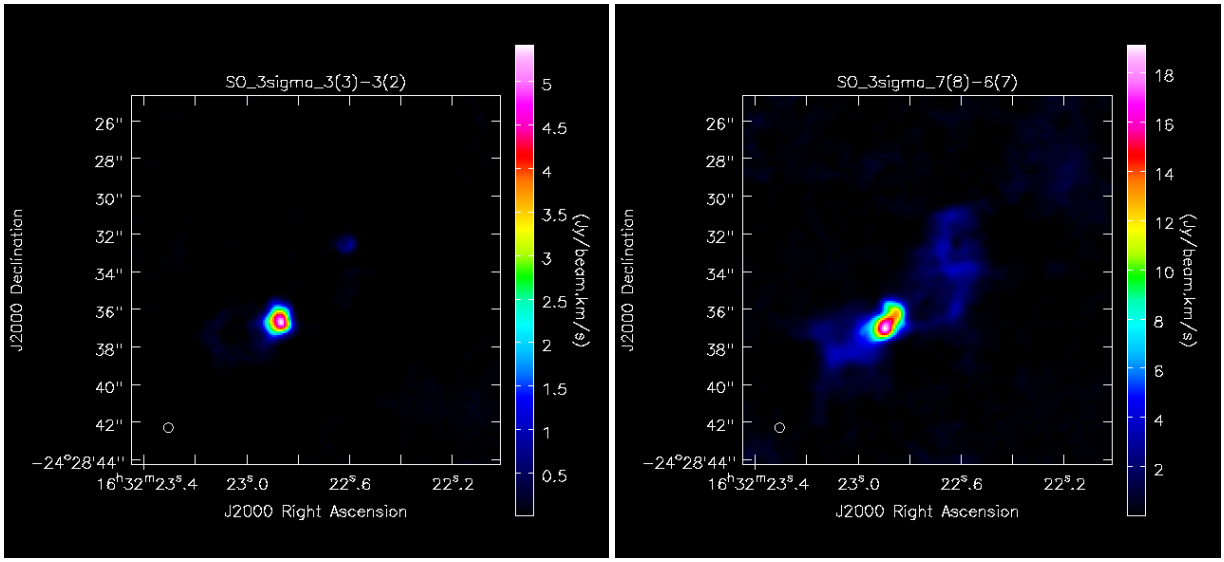

Figure 3.15: *SO* 3Σ $3(3)-3(2)$ and *SO* 3Σ $7(8)-6(7)$ Moment 0 maps. $7(8)-6(7)$ transition, characterized by a higher E_u, shows an elongated structure along NE-SW direction.

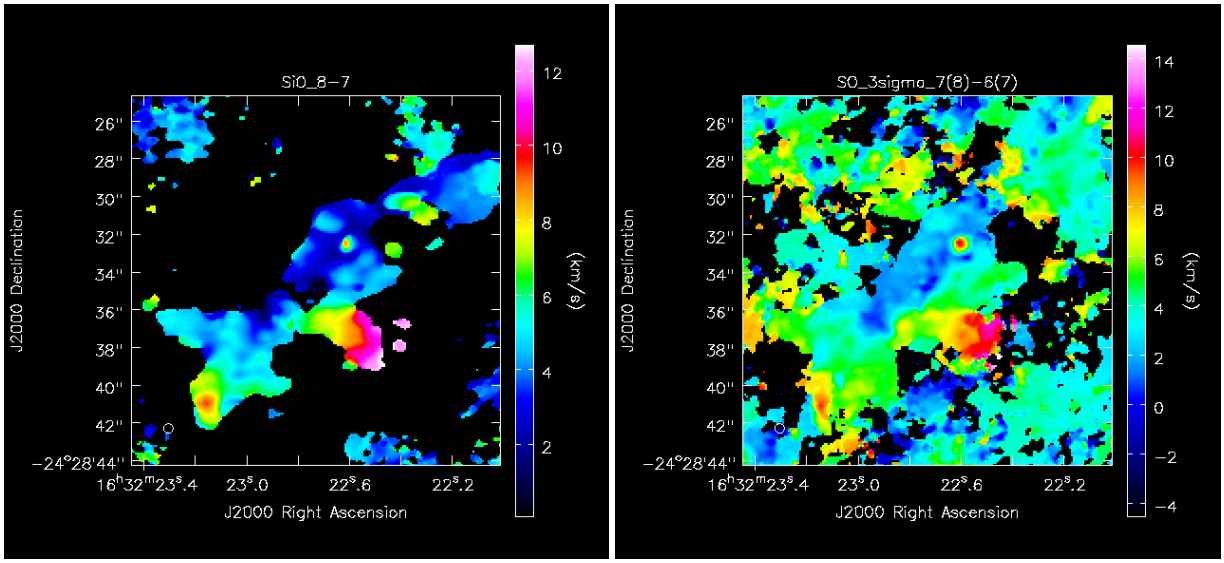

Figure 3.16: *SiO* $8-7$ and *SO* 3Σ $7(8)-6(7)$ Moment 1 maps. They show similar velocity distribution.

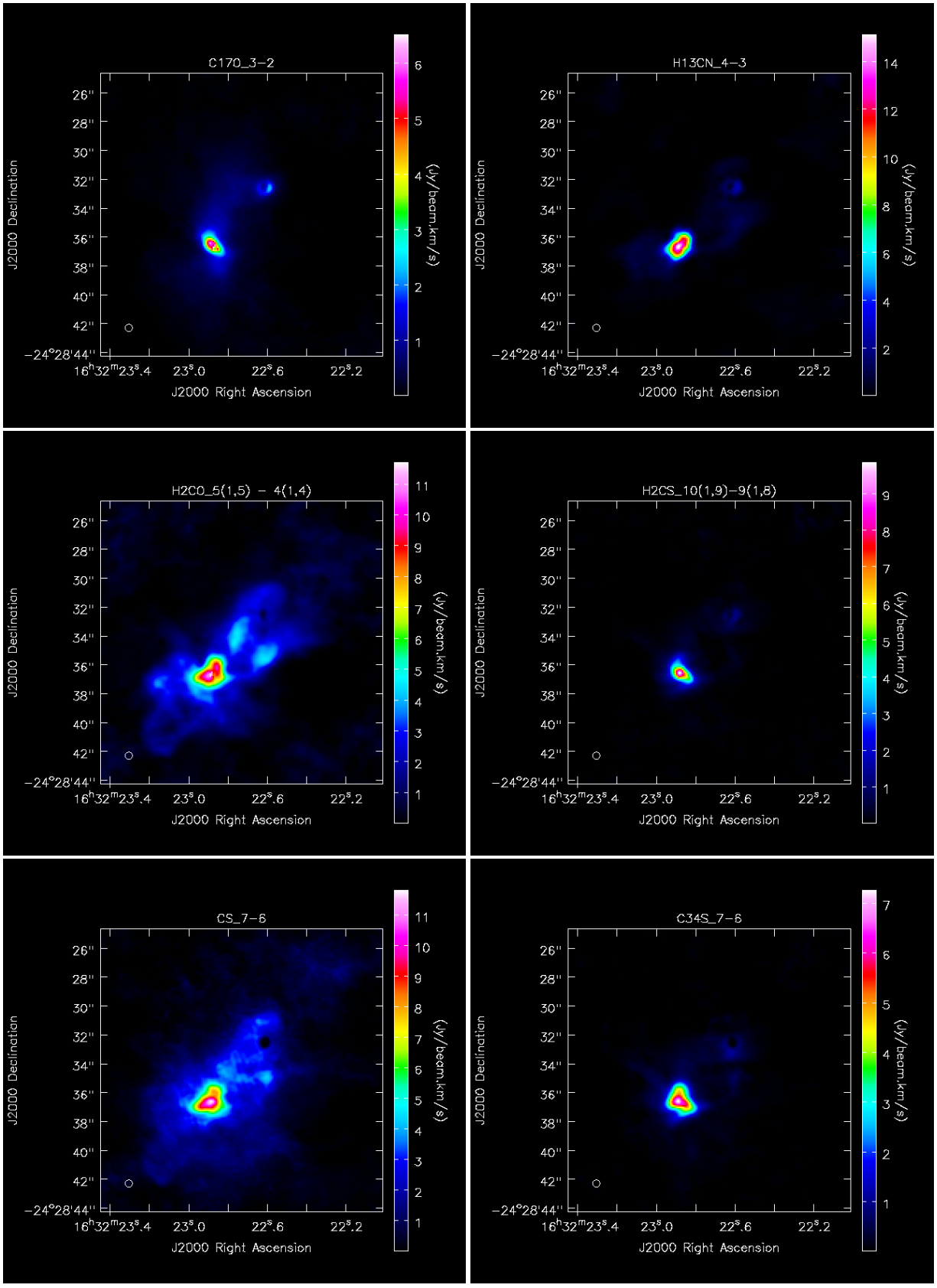

Figure 3.17: Moment 0 maps for transitions observed also in the envelope.

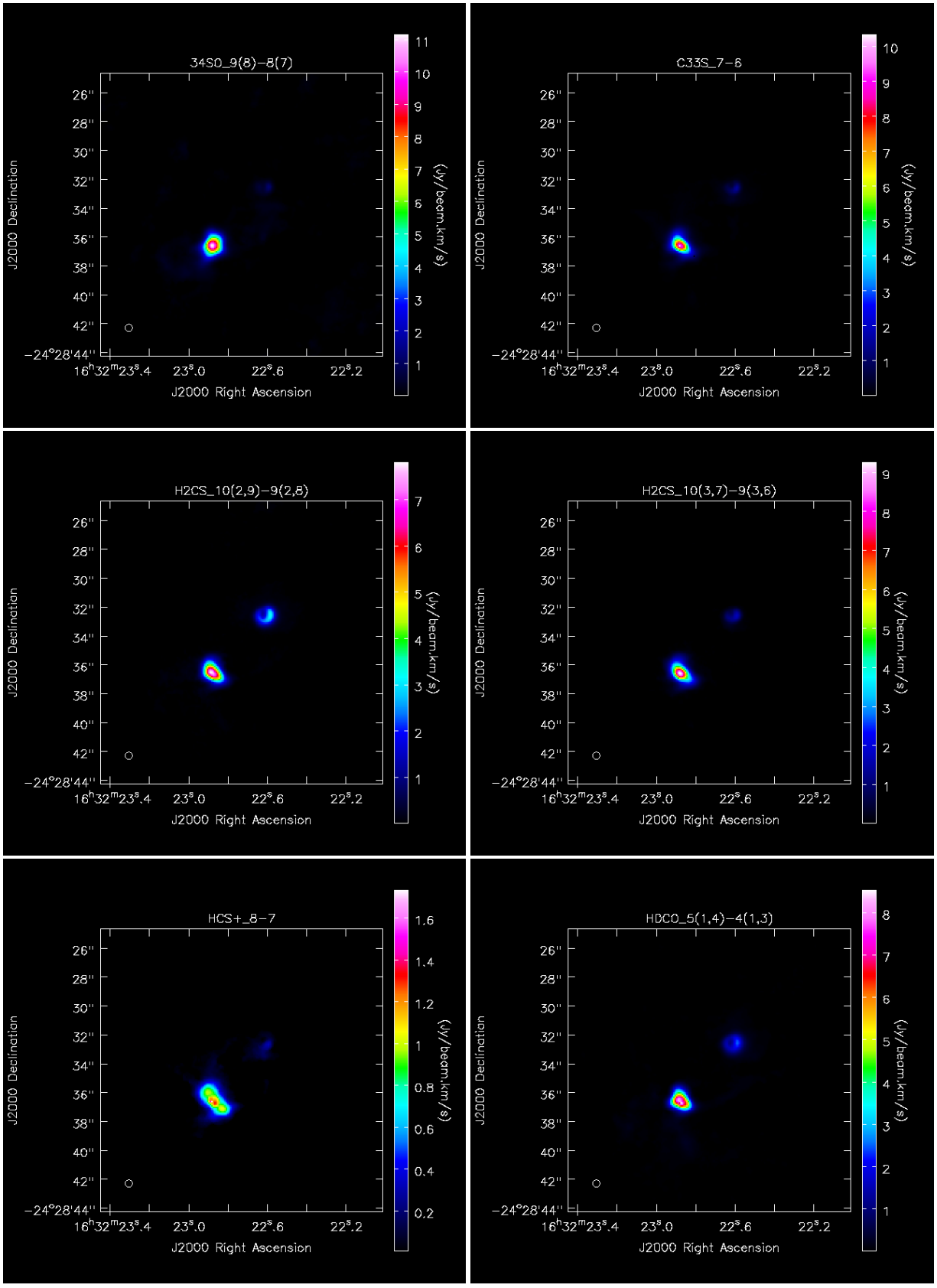

Figure 3.18: Moment 0 maps for other transitions from different species. 1 of 2.

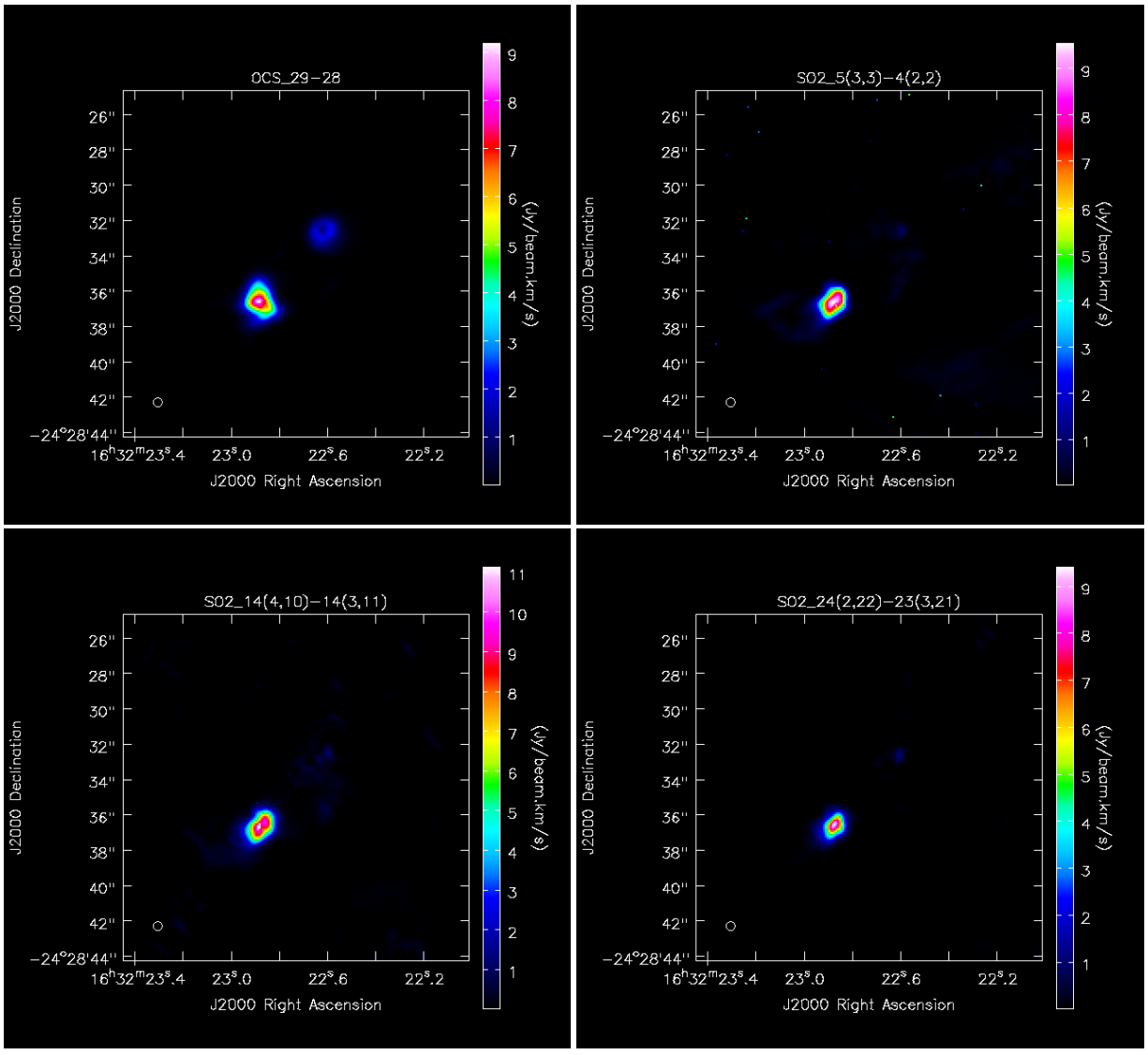

Figure 3.19: Moment 0 maps for other transitions from different species. 2 of 2.

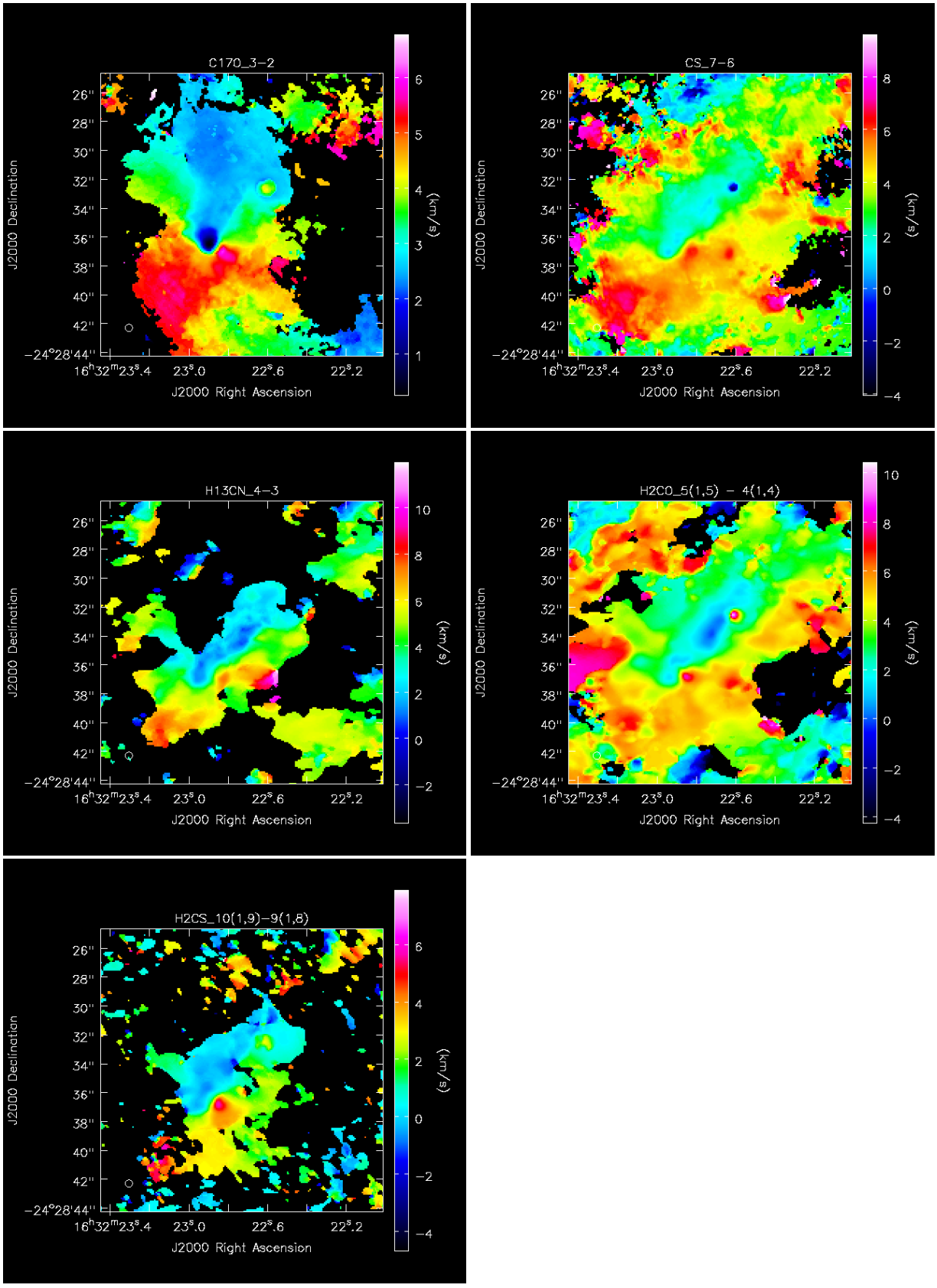

Figure 3.20: Moment 1 images showing velocity distribution probably influenced by the NE-SW outflow.

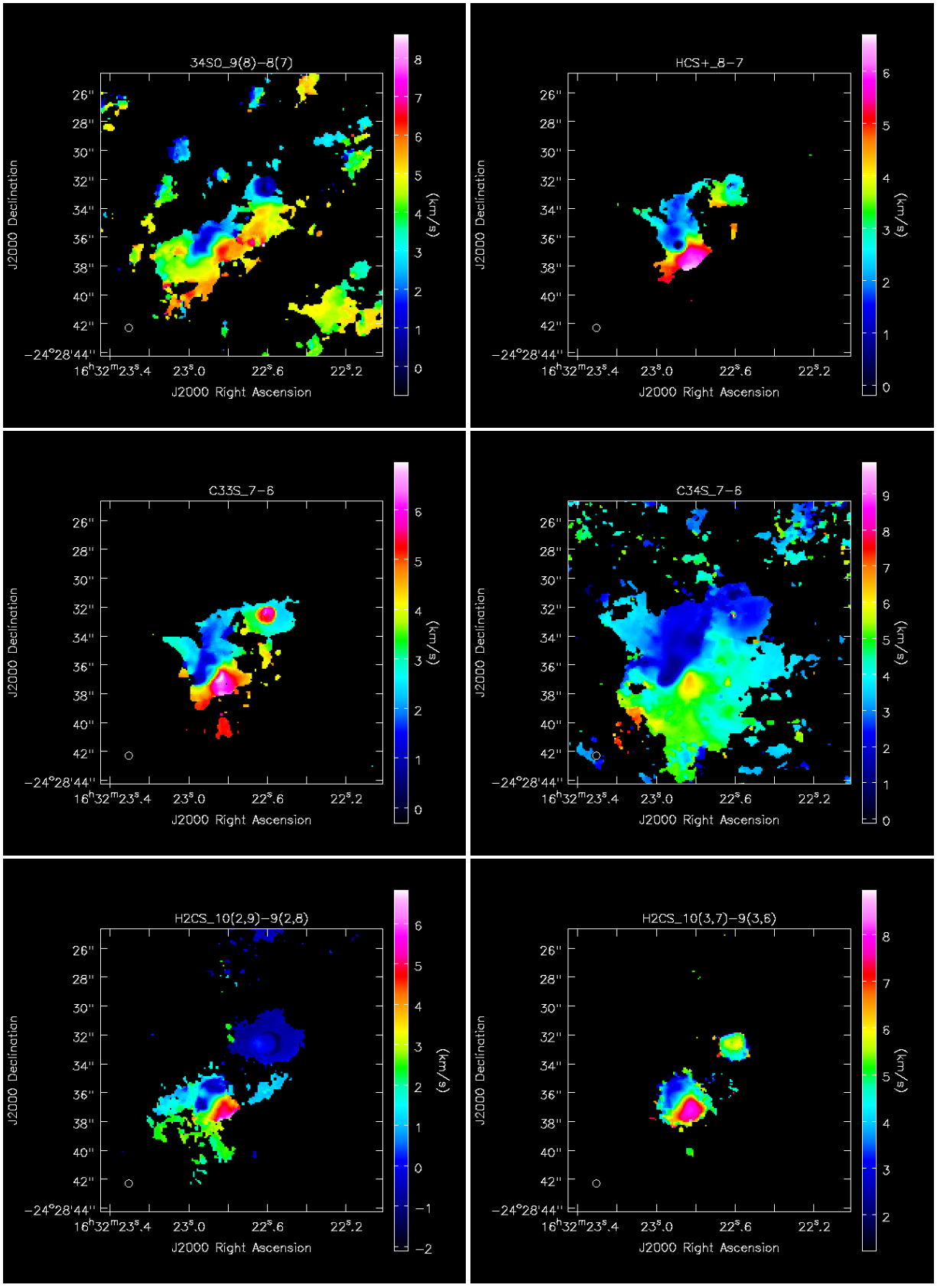

Figure 3.21: Moment 1 maps for other transitions from different species. 1 of 2.

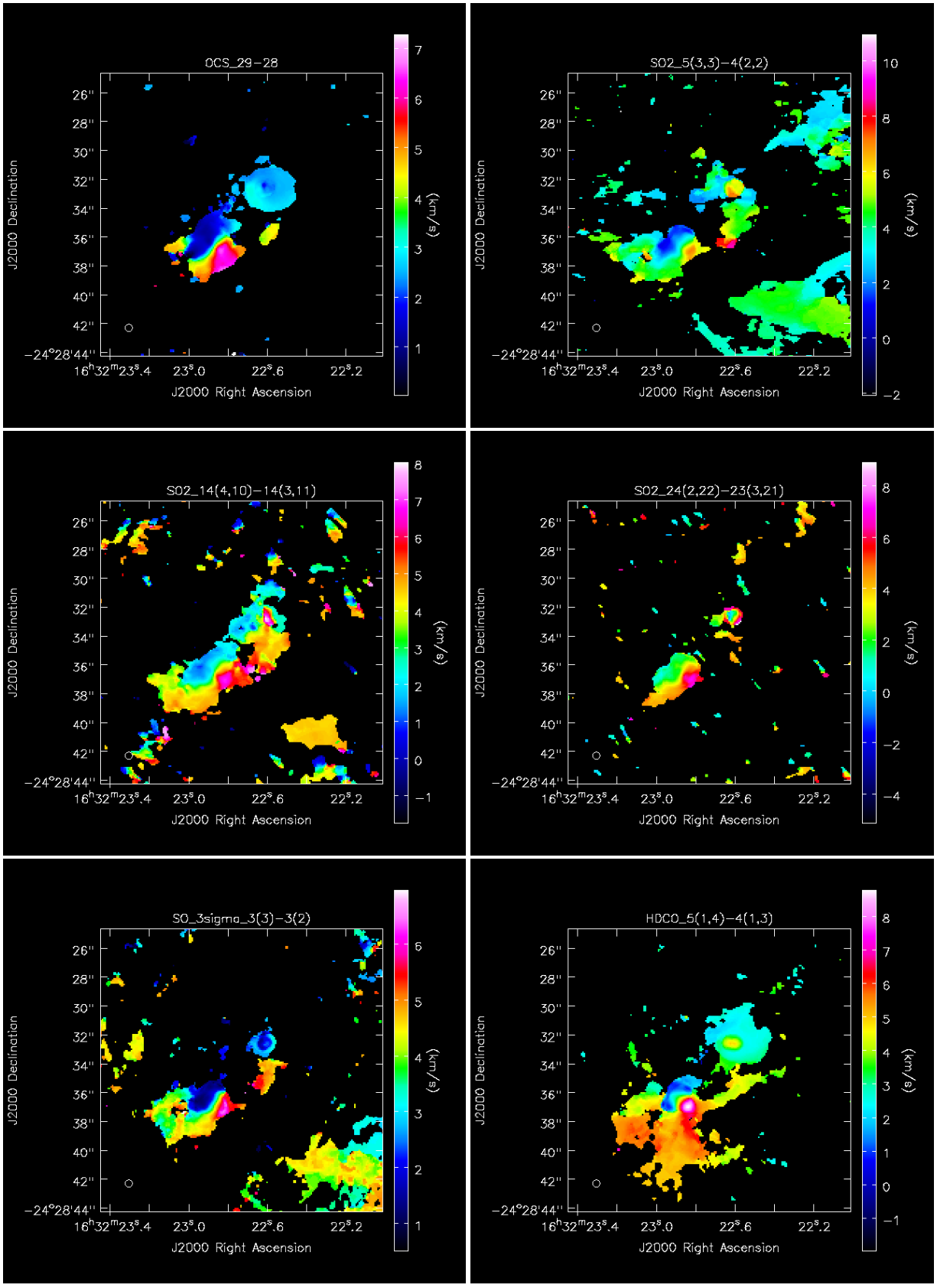

Figure 3.22: Moment 1 maps for other transitions from different species. 2 of 2.

Species & Transitions	Frequency lit. (GHz)		V_0 ($km\ s^{-1}$)	σ_{V_0}	FWHM ($km\ s^{-1}$)	σ_{FWHM}	Int ($Jy\ beam^{-1} km\ s^{-1}$)	σ_{Int}	S_{int} ($Jy\ km\ s^{-1}$)	$\sigma_{S_{int}}$
$^{34}SO\ \ 9(8)-8(7)$	339.85763	cont.px.	3.148	0.021	8.780	0.055	9.835	0.075	57.0	2.9
		br.px.	2.618	0.026	9.262	0.069	10.096	0.093		
$C^{17}O\ \ 3-2$	337.06112		0.76	0.14	5.80	0.33	4.54	0.34	45.5^a	2.3
			1.35	0.22	9.21	0.55	6.40	0.49		
$C^{33}S\ \ 7-6$	340.05258		3.54	0.11	11.28	0.28	8.84	0.28	39.2	2.0
			2.73	0.13	11.74	0.31	10.05	0.35		
$C^{34}S\ \ 7-6$	337.39646		2.668	0.067	8.09	0.16	7.02	0.18	69.3^b	3.5
			1.664	0.057	6.20	0.14	7.49	0.22		
$CS\ \ 7-6$	342.88285		2.29	0.23	10.20	0.56	11.49	0.82	103.6^c	5.2
			1.471	0.095	6.71	0.22	10.98	0.48		
$H_2CO\ \ 5(1,5)-4(1,4)$	351.76864		5.03	0.51	13.4	1.3	8.8	1.1	101.0^c	5.0
			2.17	0.17	8.07	0.40	10.68	0.69		
$H_2CS\ \ 10(1,9)-9(1,8)$	348.53187		2.904	0.038	8.125	0.091	9.22	0.14	63.2	3.2
			1.289	0.044	7.89	0.11	9.86	0.17		
$H_2CS\ \ 10(2,9)-9(2,8)$	343.32208		2.166	0.054	8.50	0.13	7.78	0.16	35.6	1.8
			0.22	0.11	7.42	0.27	7.52	0.36		
$H_2CS\ \ 10(3,7)-9(3,6)$	343.41415		5.864	0.060	10.06	0.16	10.15	0.20	38.9	1.9
			5.204	0.073	10.20	0.20	10.07	0.24		
$H^{13}CN\ \ 4-3$	345.33977		4.420	0.095	11.89	0.25	15.08	0.39	112.3^d	5.6
			2.776	0.078	9.54	0.19	15.07	0.39		
$HCS+\ \ 8-7$	341.35023		1.303	0.079	5.22	0.19	1.273	0.060	11.39	0.57
			0.79	0.12	7.23	0.29	1.777	0.093		
$HDCO\ \ 5(1,4)-4(1,3)$	335.09678		5.18	0.12	11.67	0.31	8.53	0.29	36.4	1.8
			5.78	0.10	12.24	0.26	9.04	0.25		
$OCS\ \ 29-28$	352.59957		2.900	0.072	8.06	0.17	8.31	0.23	66.0	3.3
			1.792	0.051	6.55	0.12	9.07	0.22		
$SiO\ \ 8-7$	347.33063		3.785	0.076	6.80	0.20	3.57	0.13	89.1^b	4.5
			3.963	0.059	5.06	0.15	5.42	0.20		
$SO_2\ \ 5(3,3)-4(2,2)$	351.25722		3.679	0.048	7.20	0.11	9.23	0.19	57.1	2.9
			3.252	0.049	7.27	0.12	9.24	0.19		
$SO_2\ \ 14(4,10)-14(3,11)$	351.87387		3.177	0.031	6.560	0.072	8.77	0.13	75.3	3.8
			2.935	0.057	7.45	0.13	10.83	0.26		
$SO_2\ \ 24(2,22)-23(3,21)$	348.3878		3.574	0.063	7.03	0.15	8.57	0.24	36.3	1.8
			3.119	0.050	6.66	0.12	8.83	0.21		
$SO\ \ 3\Sigma\ \ 3(3)-3(2)$	339.34146		2.941	0.053	7.11	0.13	5.40	0.13	27.1	1.4
			3.925	0.093	7.38	0.23	5.50	0.22		
$SO\ \ 3\Sigma\ \ 7(8)-6(7)$	340.71416		2.802	0.059	10.30	0.14	15.62	0.28	136.5^e	6.8
			1.935	0.079	9.15	0.19	19.09	0.51		

Table 3.6: Statistics obtained from gaussian fits for different species I examined. Uncertainties on flux densities are given by 2.3. V_0 = Gauss Center, Int = Gauss Area. cont.px. = continuum peak pixel, br.px. = brightest pixel.
a: Flux density calculated inside a 8.5σ contour. See §2.2.1.
b: Flux density calculated inside a 5σ contour.
c: Flux density calculated inside a 44σ contour.
d: Flux density calculated inside a 4σ contour.
e: Flux density calculated inside a 20σ contour.

Chapter 4

Conclusions

From my data analysis on this system I have highlighted the fact that the emission from all species is influenced by the presence of outflows.
All species, both those which emit only from a compact region (the hot corino) and those which also present a significant emission from the envelope, peak close to the continuum peak. However, as can be seen in Figure 3.13, lines' peaks show an offset from the continuum peak towards South West, providing an evidence that the emission of all species could be influenced by the NE-SW outflow. This outflow, mentioned already in previous studies, is here clearly traced by integrated emission map of SiO $8-7$. SiO is indeed generally considered as an outflow tracer. Thus, I also deduced the influence of NE-SW outflow on velocity distributions of some species (CO, CS, H_2CO, H_2CS, $H^{13}CN$, SO and CH_3OH) since they resemble the one from SiO. Moreover, as an additional proof of the effect of the NE-SW outflow on it, SO 3Σ $7(8)-6(7)$ integrated emission shows an elongated structure along that direction.

From Moment 0 maps I realized in this project it is also possible to notice that species like CS, H_2CS, HCN and SO, which in previous studies were considered to be located only toward Source A, are instead also located toward the envelope.

I have also evidenced that methanol emission is concentrated mainly in a compact region around the protostar, about 140×110 AU large, where the temperature is high enough to let the methanol sublimate from dust grains' mantles.
Methanol and ^{13}methanol are not only influenced by NW-SW outflow. As shown from their temperature distribution in Figure 3.2, the cloud in which methanol is contained is warmer in two regions along E-W direction. Thus it could be an evidence that this cloud is heated from the shocks caused by an E-W outflow whom existence has been reported in previous studies. So, in this case, the central protostar is not the only source of heat for the gas cloud (if it was, there must have been a temperature gradient towards the center). The same shocks generated from E-W outflow could also be responsible of the elongated

shape of methanol emission along E-W direction, in the lower part of methanol emission, where they may cause sputtering of dust grains and release of methanol in the gas phase. This scenario is supported also from the observed blueshift (in the western warm region) and redshift (in the eastern one) of methanol lines.

From this work it has been pointed out how both the heating from the central protostar and the outflows influence the distribution of molecular emission. As previously said from methanol compact emission we understand how only regions close enough to the central protostar are characterized by a dust temperature high enough to let methanol pass to the gas phase and emit lines which we are able to detect. But heating can also be provided by outflows as it happens for methanol and E-W outflow. Moreover, the fact that most species peak at a significant distance from the central protostar make us understand that the heat brought from outflows also enhances the emission of molecules which are already in the gas phase.

Future investigations should be held - also in this same dataset - to find out if there are other transitions like $C^{17}O \;\; 3-2$ and $HCS+ \;\; 8-7$ which don't show the SW offset and see if these species are somehow related and why.
The existence of two outflows could be related to the fact that the continuum source, at certain wavelengths, results to be split in two sources. In fact, outflows formation is related to the loss of angular momentum from the disk and the protostar, and an outflow perpendicular to the disk should therefore be generated. This - considering the observed disk orientation and velocity gradients - would explain the existence of NE-SW outflow, but not the existence of the E-W outflow. Thus, perhaps using the same method I used, it should be a good idea also to verify if there are other species that, like methanol, are heated by the E-W outflow or the NE-SW outflow; this could maybe lead to a better understanding of their formation mechanism and therefore provide an explanation to this question.

Acknowledgements

I would like to thank my supervisors Jes Jørgensen and Matthijs van der Wiel for their thorough guidance through my work in this project and for allowing me to work in such a great environment as StarPlan during this wonderful exchange period in Copenhagen. Many thanks also to Lars Kristensen, Elizabeth Arthur and Hannah Calcutt for their precious suggestions.

Thanks to my supervisor at University of Bologna, Andrea Cimatti, for his support.

Thanks to my *Laundry Family*; their love, friendship and - later - absence have been with me every day while working at this thesis. Thank you all for having made my stay in Copenhagen unforgettable.

And, last but not least, many thanks to my family and my old friends which never stopped supporting me.

References

André, P., Ward-Thompson, D. & Barsony, M. 1993, ApJ, 406, 122

Bacmann, A., Taquet, V., Faure, A., Kahane, C., Ceccarelli, C. 2012, A&A, 541, L12

Caselli, P. & Ceccarelli, C. 2012, A&A Rev, 20

Caux, E., Kahane, C., Castets, A., et al. 2011, A&A, 532, A23

Chandler, C. J., Brogan, C. L., Shirley, Y. L., & Loinard, L. 2005, ApJ, 632, 371

Correia, J. C., Griffin, M., & Saraceno, P. 2004, A&A, 418, 607

Crimier, N., Ceccarelli, C., Maret, S., et al. 2010, A&A, 519, A65

Goldsmith, P. F., Langer,W. D., & Velusamy, T. 1999, ApJ, 519, L173

Jørgensen, J. K., Bourke, T. L., Nguyen Luong, Q., Takakuwa, S. 2011, A&A, 534, A100

Jørgensen, J. K., Favre, C., Bisschop, S. E., et al. 2012, ApJ, 757, L4

Jørgensen, J. K., van der Wiel, M. H. D., Coutens, A., et al. 2016, A&A, in press (arXiv:1607.08733)

Keto, E., Caselli, P. 2008, ApJ, 683, 238-247

Lada, C. J. 1999, *The Formation of Low Mass Stars*

Loinard, L., Torres, R. M., Mioduszewski, A. J., & Rodríguez, L. F. 2008, ApJ, 675, L29

Loinard, L., Zapata, L. A., Rodríguez, L. F., et al. 2013, MNRAS, 430, L10

Milam, S. N., Savage, C., Brewster, M. A., Ziurys, L. M., & Wyckoff, S. 2005, ApJ, 634, 1126

Pineda, J. E., Maury, A. J., Fuller, G. A., et al. 2012, A&A, 544, L7

Schöier, F. L., Jørgensen, J. K., van Dishoeck, E. F., & Blake, G. A. 2004, A&A, 418, 185

Stahler, S. & Palla, F., *The Formation of Stars*, 2004, WILEY-VCH Verlag, Weinheim

Tielens, A.G.G.M. & Hagen, W. 1982, A&A, 114, p. 245 Van der Tak, F.F.S., Black, J.H., Schöier, F.L., Jansen, D.J., van Dishoeck, E.F. 2007, A&A, 468, 627-635

Van Dishoeck, E. F. & Hogerheijde, M. R. 1999, *Models and Observations of the Chemistry Near Young Stellar Objects*

Van Dishoeck, E. F. 2014, Faraday Discuss.,168, 9-47 Wootten, A. 1989, ApJ, 337, 858

Oya, Y., Sakai, N., López-Sepulcre, A., et al. 2016, ApJ, 824, 88

Appendix A:
Radex simulation outputs

Radex simulation outputs respectively for a-methanol and e-methanol:

```
* Radex version        : 30nov2011
* Geometry             : Uniform sphere
* Molecular data file  : /home/francesco/Radex/data/a-ch3oh.dat
* T(kin)           [K]:   93.700
* Density of H2  [cm-3]:  1.000E+12
* T(background)    [K]:    2.730
* Column density [cm-2]:  3.000E+18
* Line width     [km/s]:    7.000
Calculation finished in   11 iterations
      LINE         E_UP       FREQ        WAVEL     T_EX      TAU        T_R      FLUX        FLUX
                   (K)        (GHz)       (um)      (K)                  (K)     (K*km/s) (erg/cm2/s)
12_2   -- 11_3     218.8    329.6329    909.4738   93.700  6.579E+00  8.585E+01  6.397E+02  2.950E-04
11_-1  -- 11_0     169.0    331.5023    904.3450   93.701  3.333E+01  8.592E+01  6.403E+02  3.003E-04
7_-3   -- 8_-1     114.8    332.9208    900.4918   93.699  2.259E-05  1.940E-03  1.446E-02  6.870E-09
2_-2   -- 3_-1      44.7    335.1336    894.5462   93.699  3.643E+00  8.360E+01  6.229E+02  3.020E-04
7_1    -- 6_1       79.0    335.5820    893.3508   93.700  4.598E+01  8.583E+01  6.396E+02  3.113E-04
14_7   -- 15_6     488.2    336.4382    891.0773   93.723  2.491E-01  1.893E+01  1.410E+02  6.916E-05
14_-7  -- 15_-6    488.2    336.4382    891.0773   93.723  2.491E-01  1.893E+01  1.410E+02  6.916E-05
12_-1  -- 12_0     197.1    336.8651    889.9480   93.701  2.698E+01  8.581E+01  6.394E+02  3.148E-04
7_0    -- 6_0       65.0    338.4087    885.8887   93.700  5.495E+01  8.577E+01  6.391E+02  3.190E-04
7_6    -- 6_6      258.7    338.4424    885.8006   93.700  1.851E+00  7.230E+01  5.387E+02  2.689E-04
7_-6   -- 6_-6     258.7    338.4424    885.8006   93.700  1.851E+00  7.230E+01  5.387E+02  2.689E-04
7_5    -- 6_5      202.9    338.4863    885.6856   93.700  6.212E+00  8.560E+01  6.378E+02  3.186E-04
7_-5   -- 6_-5     202.9    338.4863    885.6856   93.700  6.212E+00  8.560E+01  6.378E+02  3.186E-04
7_-4   -- 6_-4     145.3    338.5126    885.6168   93.700  1.573E+01  8.577E+01  6.391E+02  3.192E-04
7_4    -- 6_4      145.3    338.5126    885.6167   93.700  1.573E+01  8.577E+01  6.391E+02  3.192E-04
7_-2   -- 6_-2     102.7    338.5129    885.6162   93.700  3.396E+01  8.577E+01  6.391E+02  3.193E-04
7_3    -- 6_3      114.8    338.5408    885.5430   93.700  2.633E+01  8.577E+01  6.391E+02  3.193E-04
7_-3   -- 6_-3     114.8    338.5432    885.5369   93.700  2.633E+01  8.577E+01  6.391E+02  3.193E-04
7_2    -- 6_2      102.7    338.6398    885.2842   93.700  3.398E+01  8.577E+01  6.391E+02  3.196E-04
2_2    -- 3_1       44.7    340.1411    881.3766   93.699  3.703E+00  8.362E+01  6.231E+02  3.158E-04
7_-1   -- 6_-1      80.1    341.4156    878.0865   93.700  4.629E+01  8.570E+01  6.386E+02  3.274E-04
13_-1  -- 13_0     227.5    342.7298    874.7196   93.701  2.118E+01  8.568E+01  6.384E+02  3.311E-04
5_-4   -- 6_-3     115.2    346.2027    865.9448   93.702  2.887E+00  8.083E+01  6.023E+02  3.219E-04
5_4    -- 6_3      115.2    346.2043    865.9410   93.702  2.887E+00  8.083E+01  6.023E+02  3.218E-04
14_-1  -- 14_0     260.2    349.1070    858.7409   93.701  1.613E+01  8.554E+01  6.374E+02  3.493E-04
1_1    -- 0_0       16.8    350.9051    854.3406   93.700  3.339E+01  8.550E+01  6.371E+02  3.545E-04
8_2    -- 9_0      121.3    351.6855    852.4448   93.700  3.027E-04  2.587E-02  1.928E-01  1.080E-07
10_4   -- 11_2     208.0    355.2795    843.8213   93.702  1.091E-03  9.315E-02  6.941E-01  4.009E-07
13_0   -- 12_1     211.0    355.6029    843.0539   93.699  1.408E+01  8.539E+01  6.363E+02  3.684E-04
15_-1  -- 15_0     295.3    356.0072    842.0965   93.701  1.193E+01  8.538E+01  6.362E+02  3.697E-04
10_-4  -- 11_-2    208.0    356.8958    839.9999   93.702  1.097E-03  9.359E-02  6.974E-01  4.082E-07
7_3    -- 8_1      114.8    362.9274    826.0398   93.699  2.482E-05  2.115E-03  1.576E-02  9.704E-09
```

```
* Radex version        : 30nov2011
* Geometry             : Uniform sphere
* Molecular data file  : /home/francesco/Radex/data/e-ch3oh.dat
* T(kin)           [K]:   93.700
* Density of H2  [cm-3]:  1.000E+12
* T(background)    [K]:    2.730
* Column density [cm-2]:  3.000E+18
* Line width     [km/s]:    7.000
Calculation finished in   11 iterations
```

LINE	E_UP (K)	FREQ (GHz)	WAVEL (um)	T_EX (K)	TAU	T_R (K)	FLUX (K*km/s)	FLUX (erg/cm2/s)
14_1 -- 14_-1	264.8	330.2301	907.8290	93.699	3.140E-03	2.695E-01	2.008E+00	9.312E-07
8_-3 -- 9_-2	146.3	330.7939	906.2817	93.696	8.647E+00	8.592E+01	6.402E+02	2.984E-04
15_1 -- 15_-1	299.6	332.5054	901.6167	93.699	2.282E-03	1.958E-01	1.459E+00	6.909E-07
9_1 -- 8_-2	125.5	333.8647	897.9459	93.698	1.769E-01	1.392E+01	1.037E+02	4.973E-05
11_0 -- 10_2	166.0	334.9706	894.9814	93.701	6.092E-03	5.214E-01	3.885E+00	1.880E-06
3_2 -- 2_0	36.2	335.1217	894.5778	93.700	4.695E-04	4.029E-02	3.002E-01	1.455E-07
7_3 -- 8_0	112.7	335.3626	893.9354	93.702	1.744E-02	1.484E+00	1.106E+01	5.373E-06
10_-3 -- 11_1	190.4	335.6040	893.2924	93.698	1.969E-05	1.690E-03	1.259E-02	6.130E-09
3_3 -- 4_2	61.6	337.1359	889.2334	93.702	2.484E+00	7.864E+01	5.860E+02	2.892E-04
7_0 -- 6_0	78.1	338.1245	886.6334	93.700	4.769E+01	8.578E+01	6.392E+02	3.182E-04
7_-1 -- 6_-1	70.6	338.3446	886.0566	93.700	5.072E+01	8.577E+01	6.391E+02	3.188E-04
7_6 -- 6_6	243.8	338.4046	885.8995	93.701	2.164E+00	7.592E+01	5.657E+02	2.823E-04
7_-6 -- 6_-6	253.9	338.4310	885.8304	93.700	1.951E+00	7.359E+01	5.483E+02	2.737E-04
7_-5 -- 6_-5	189.0	338.4565	885.7635	93.700	7.172E+00	8.570E+01	6.386E+02	3.189E-04
7_5 -- 6_5	201.1	338.4752	885.7146	93.700	6.309E+00	8.561E+01	6.379E+02	3.186E-04
7_-4 -- 6_-4	152.9	338.5041	885.6392	93.700	1.448E+01	8.577E+01	6.391E+02	3.192E-04
7_4 -- 6_4	161.0	338.5303	885.5706	93.700	1.336E+01	8.577E+01	6.391E+02	3.193E-04
7_-3 -- 6_-3	127.7	338.5600	885.4929	93.700	2.310E+01	8.577E+01	6.391E+02	3.195E-04
7_3 -- 6_3	112.7	338.5832	885.4321	93.700	2.701E+01	8.577E+01	6.391E+02	3.195E-04
7_1 -- 6_1	86.1	338.6149	885.3492	93.700	4.407E+01	8.577E+01	6.391E+02	3.196E-04
7_2 -- 6_2	87.3	338.7217	885.0701	93.700	3.941E+01	8.576E+01	6.391E+02	3.198E-04
7_-2 -- 6_-2	90.9	338.7229	885.0670	93.700	3.835E+01	8.576E+01	6.391E+02	3.199E-04
5_-2 -- 4_1	60.7	343.0059	874.0155	93.702	2.633E-02	2.226E+00	1.659E+01	8.622E-06
14_-1 -- 13_1	248.9	346.7828	864.4964	93.701	4.210E-03	3.596E-01	2.679E+00	1.439E-06
2_2 -- 2_-1	29.2	347.2716	863.2796	93.700	1.181E-04	1.010E-02	7.529E-02	4.060E-08
3_2 -- 3_-1	36.2	347.3003	863.2082	93.700	6.934E-04	5.932E-02	4.420E-01	2.384E-07
4_2 -- 4_-1	45.5	347.3700	863.0349	93.700	2.094E-03	1.790E-01	1.334E+00	7.200E-07
5_2 -- 5_-1	57.1	347.5075	862.6936	93.700	4.316E-03	3.685E-01	2.746E+00	1.484E-06
6_2 -- 6_-1	71.0	347.7454	862.1032	93.700	6.669E-03	5.688E-01	4.238E+00	2.296E-06
7_2 -- 7_-1	87.3	348.1225	861.1693	93.700	7.917E-03	6.747E-01	5.028E+00	2.732E-06
8_2 -- 8_-1	105.8	348.6820	859.7877	93.700	6.953E-03	5.927E-01	4.417E+00	2.411E-06
13_0 -- 12_-2	223.8	348.8236	859.4386	93.699	3.536E-03	3.020E-01	2.250E+00	1.230E-06
10_3 -- 11_-1	175.4	348.9955	859.0153	93.702	1.442E-06	1.233E-04	9.189E-04	5.030E-10
9_2 -- 9_-1	126.7	349.4700	857.8488	93.700	3.831E-03	3.270E-01	2.437E+00	1.340E-06
10_2 -- 10_-1	150.0	350.5344	855.2439	93.700	5.437E-04	4.647E-02	3.463E-01	1.921E-07
4_0 -- 3_-1	36.3	350.6877	854.8703	93.700	2.130E+01	8.550E+01	6.371E+02	3.538E-04
9_5 -- 10_4	240.5	351.2365	853.5345	93.696	2.134E+00	7.537E+01	5.616E+02	3.134E-04
11_2 -- 11_-1	175.5	351.9215	851.8732	93.700	9.834E-04	8.401E-02	6.260E-01	3.514E-07
12_2 -- 12_-1	203.4	353.6732	847.6539	93.700	9.785E-03	8.319E-01	6.199E+00	3.531E-06
13_2 -- 13_-1	233.6	355.8244	842.5293	93.699	3.035E-02	2.552E+00	1.902E+01	1.103E-05
9_-3 -- 10_2	167.2	358.2009	836.9394	93.698	6.992E-03	5.946E-01	4.431E+00	2.622E-06
14_2 -- 14_-1	266.1	358.3996	836.4754	93.699	6.285E-02	5.198E+00	3.873E+01	2.296E-05
10_6 -- 11_5	306.4	358.4146	836.4403	93.713	1.058E+00	5.573E+01	4.153E+02	2.463E-04
4_1 -- 3_0	44.3	358.6058	835.9945	93.700	2.854E+01	8.533E+01	6.358E+02	3.775E-04
9_2 -- 8_-2	126.7	359.4062	834.1327	93.698	3.055E-03	2.602E-01	1.939E+00	1.160E-06
11_0 -- 10_1	166.0	360.8489	830.7977	93.701	1.798E+01	8.528E+01	6.354E+02	3.845E-04
15_2 -- 15_-1	301.0	361.4113	829.5050	93.698	1.033E-01	8.366E+00	6.234E+01	3.790E-05
8_1 -- 7_2	104.6	361.8522	828.4942	93.700	1.627E+01	8.525E+01	6.353E+02	3.876E-04
3_3 -- 4_1	61.6	362.0694	827.9973	93.702	1.267E-03	1.079E-01	8.041E-01	4.916E-07
2_-2 -- 1_0	32.9	362.9082	826.0834	93.701	2.416E-04	2.059E-02	1.535E-01	9.445E-08

Appendix B:
Line blending toward Source A

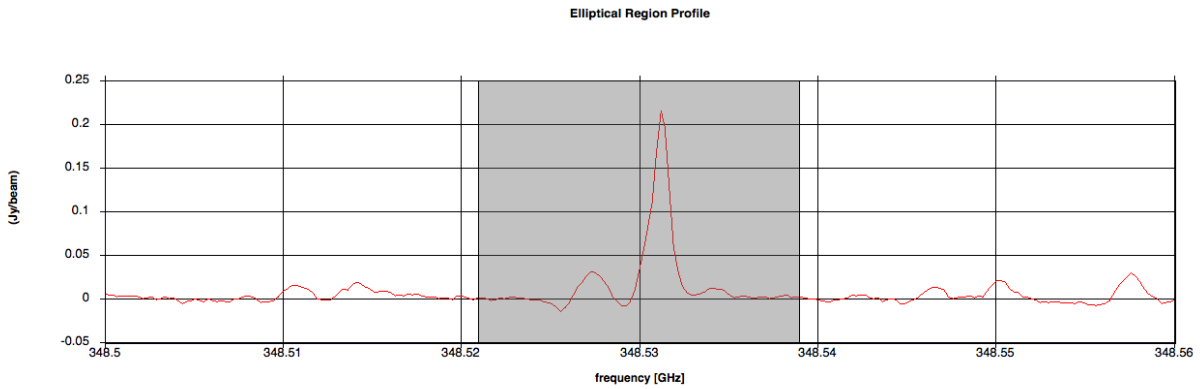

Figure 4.1: The highlighted (in grey) band is as wide as H_2CS $10(1,9)-9(1,8)$ in Source A spectrum. From this Figure one can see how, towards Source B, the same band encloses also another small line besides H_2CS $10(1,9)-9(1,8)$ (the bigger one).

When I realized Moment maps, I obtained them by integrating over a band enclosing the whole width of the line in question belonging to Source A spectrum. But if we consider the same bandwidth for the spectrum extracted from Source B, that often encloses - besides the line in question - also other less intense lines, as it is shown in Figure 4.1. This happens because lines toward Source A are much wider than those toward Source B ($\approx$7-10 km/s vs $\approx$1.5 km/s). It means that, looking for example at Figure 4.1, what I see as a H_2CS $10(1,9)-9(1,8)$ single wide line toward Source A may also contain small contribution from an other small line which can be distinguished in Source B spectrum. This happens for many lines I analyzed, but other lines' contributions are usually as small as shown in this figure or even smaller and, anyway, it is not possible to quantify them: I can measure the line ratios between the lines in a band for Source B spectrum but that doesn't mean that those ratios have the same value toward Source A.